

Multiresolution analysis for material design

Cahal McVeigh, Franck Vernerey, Wing Kam Liu *, L. Cate Brinson

Department of Mechanical Engineering, Northwestern University, Evanston, IL 60208, United States

Received 9 May 2005; received in revised form 26 June 2005; accepted 5 July 2005

Abstract

The relationship between material microstructure and properties is the key to optimization and design of lightweight, strong, tough materials. Material properties are inherently a function of the microscale interactions at each distinct scale of deformation in a material. Currently, we rely on empirical data to define the structure–property link in the material design chain. A model is proposed here in which a material is physically and mathematically decomposed to each individual scale of interest. Material deformation can subsequently be resolved to each of these scales. Constitutive behavior at each scale can be determined by analytically or computationally examining the micromechanics at each scale. This is illustrated for a polycrystalline material, a granular material, a porous material and an alloy containing particles at two scales. A potential use for a bio-inspired self-healing composite is also discussed. The theory can then be applied computationally in a finite element framework to determine the overall material properties in terms of the constitutive behavior at each scale, without resorting to empiricism.

© 2005 Elsevier B.V. All rights reserved.

Keywords: Multiresolution; Multiscale; Material design; Constitutive law; Alloy

1. Introduction

Over the previous centuries there have been significant experimental and theoretical accomplishments in the development of materials science and engineering, chemistry, and physics. However, a consistent and reliable technique for the design of materials has remained an elusive goal.

Fig. 1 represents the life of a component from the initial processing of the raw material, to resulting material microstructure, the subsequent properties and the final product's performance. Material scientists focus on the relationship between processing and the resulting microstructure. Specialized imaging techniques such as scanning electron microscopy (SEM) or tunneling electron microscopy (TEM) are utilized to characterize the microstructure. Over the years, designers have gathered extensive amounts of experimental data relating processing parameters, such as processing temperature and deformation rate, to the final microstructure. The relationship between processing parameters and microstructure is well understood for traditional processing techniques such as extrusion [1,2] and rolling [3–5] and in new areas such as friction stir welding [6]. Processing charts and empirically based mathematical models are widely available. It is possible to 'design' a microstructure by controlling the processing parameters.

The relationship between the properties and performance is also well understood. Design engineers select materials based on performance requirements. Materials are chosen depending on their mechanical properties, density, chemical resistance and other pertinent physical characteristics. The suitability of a material for a particular application can be

* Corresponding author. Fax: +1 847 4913915.

E-mail address: w-liu@northwestern.edu (W.K. Liu).

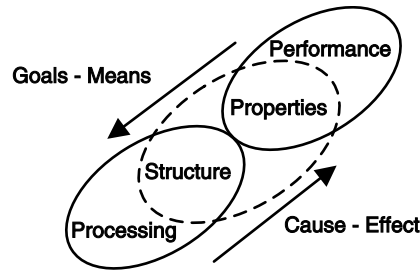


Fig. 1. From processing to performance. A general technique to determine a complex material's structure–property relationship remains elusive.

determined through the use of design charts or computationally through numerical techniques such as the finite element method [7] or other meshfree methods [8].

At an elementary level, material design is a method of linking the material processing (input) to the material performance (output). There is a cause–effect relationship associated with moving from processing to performance; changing a processing parameter will have an effect on the microstructure, properties and performance. Moving in the opposite direction, a goal–means relationship is evident; the goal is to achieve the desired performance capability by defining the needed properties, relating those to the required microstructure and ultimately choosing the correct processing technique/parameters.

1.1. Structure–property: The missing link

When designing a material for a particular application, an iterative optimization process is employed to achieve the desired properties: a material with a specific microstructure is produced and its properties, such as strength and fracture behavior, are found experimentally. A new microstructure is then devised which results in improved properties. The question remains: *what microstructure will produce the desired material properties?* For many materials, including the next generation of lightweight alloys, granular materials and self-healing composites, the relationship between microstructure and properties is vague. The general problem of calculating the inherent properties of a complex multicomponent material from the knowledge of its constituent components' properties has remained unsolved. Direct computational prediction of the behavior of complex materials by explicitly modeling each microscale component is not yet practical.

The alternative to direct simulation of a material's microstructure is the use of some degree of material homogenization i.e. averaging a material's microstructure over a macroscopic area. Homogenization is typically performed in one of several approaches. The simplest method is to experimentally load a material sample in tension, compression and torsion and record the average constitutive response. The resulting *homogenized constitutive relationship* can then be applied through a conventional continuum framework to find the resulting material properties such as toughness and strength. Homogenization infers that the microstructural constituents and the associated micromechanics are 'smeared out' over a macroscopic volume (Fig. 2a). Such models fail to provide a relationship between structure and properties. Some phenomenological and

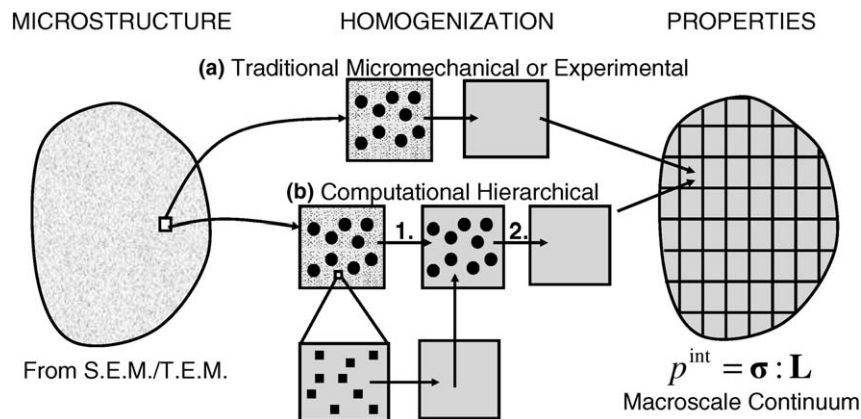


Fig. 2. Links between microstructure and properties. A material's microstructure can be determined through imaging techniques such as tunneling electron microscopy (TEM) or scanning electron microscopy (SEM). (a) Traditional micromechanical or experimental: the real microstructure is smeared out and the average behavior is recorded. (b) Hierarchical: the average behavior of the smallest scale is found through explicit computational simulations. This average behavior is used to define the matrix material at the next largest scale, and so on.

micromechanical models do take account of microstructure and small-scale phenomena such as inclusions, void growth and dislocation effects. *Phenomenological models* [9,10] take the behavior of the microstructure and smear it out to produce an averaged macroscale empirical parameter-based law. *Micromechanical models* [11,12,51–53] incorporate the microscale mechanics more directly and can capture subscale effects within macroscale models.

The *hierarchical technique* [13,43,50] (also known as serial coupling or parameter passing) is a way of injecting limited multiple scale physics into a macroscale constitutive law through a computational cell modeling technique. The average constitutive behavior at the smallest scale is used to determine the behavior at the next largest scale, and so on until the macroscale behavior is defined (Fig. 2b). These material laws are improvements on conventional homogenized constitutive relationships as they contain some microscale parameters. However, they are still used within a conventional continuum framework to determine a sample's behavior.

Conventional continuum approximations cannot capture highly localized deformation fields on the order of the microstructure's characteristic length. Also, constitutive behavior at these smaller scales is generally much different than the macroscale average behavior. As such, important material behavior cannot be explained, such as the inherent inhomogeneity of plastic deformation, plastic flow localization in shear bands and the effect of crack size and geometry on fracture behavior. These phenomena control the important mechanical behavior such as fracture toughness and strength. They must be captured to provide a link between structure and properties.

The goal here is to model a material such that *the identity of each scale of interest is maintained* i.e. a multiresolution approach. The *deformation and constitutive behavior of each scale can then be examined separately* while determining the overall material properties. In this way, the *properties are elucidated in terms of the key microstructural parameters* which control the micromechanics at each scale. This is achieved analytically or through simulation techniques, *rendering empiricism redundant*.

2. Multiresolution framework

A multiscale material is one which contains discrete microstructural constituents at N scales of interest. For example, a material may contain weakly bonded *microscale* particles and *nanoscale* dislocations. In that example, three scales are of interest: the macroscale, the microscale and the nanoscale. The material behavior of each scale will differ considerably. A model which hopes to simulate the structure–property relationship of a material must capture the micromechanics at each distinct scale. A general multiresolution framework is thus formulated in which

- the material structure and the deformation field are resolved at each scale of interest.
- The resulting internal power is a multifield expression with contributions from the average deformation at each scale i.e. the overall properties depend on the average deformation at each scale.
- The deformation behavior at each scale is found by examining the micromechanics at each scale. Constitutive relations can be developed at each scale.

2.1. Multiresolution decomposition

We begin by deriving the internal power of a simple two-scale material as shown in Fig. 3 for a material containing a metal matrix with microscale inclusions. Here, the macroscale and microscale are of interest. The goal is to resolve the material structure and deformation to the macro and microscales. The general equation for N scales is then given.

In a conventional continuum simulation, homogenized constitutive behavior at a point is predetermined by finding the average behavior of a material sample. This can be achieved through experimental mechanical testing. Alternatively, for a multicomponent material with known individual component properties, computational simulations can be performed on a

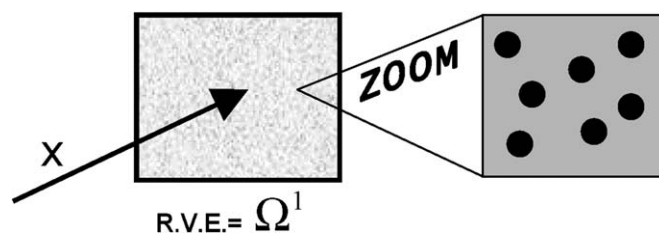


Fig. 3. A 'two-scale' material. The macroscale and microscale, which contains spherical microparticles, are of interest. The average behavior of an RVE is traditionally used to represent a point x in a continuum framework.

sample called a representative volume element (RVE) (Fig. 3). This is directly analogous to an experimental test. The stress and deformation rate averaged over the RVE are the *macrostress* and *macrodeformation rate*:

$$\bar{\boldsymbol{\sigma}}^1 = \frac{1}{V_{\text{RVE}}} \int_{V_{\text{RVE}}} \boldsymbol{\sigma} dV = \frac{1}{2V_{\text{RVE}}} \int_{S_{\text{RVE}}} \boldsymbol{\sigma} \cdot \mathbf{n} \otimes \mathbf{x} dS, \quad (1)$$

$$\bar{\mathbf{L}}^1 = \frac{1}{V_{\text{RVE}}} \int_{V_{\text{RVE}}} \mathbf{L} dV = \frac{1}{2V_{\text{RVE}}} \int_{S_{\text{RVE}}} (\mathbf{v} \otimes \mathbf{n} + \mathbf{n} \otimes \mathbf{v}) dS. \quad (2)$$

The relationship between these two quantities is a conventional homogenized constitutive law and represents the average macroscale behavior. In this paper, the RVE can be thought of as a macroscale averaging domain, Ω^1 . The deformation measure used here is the velocity gradient, $\mathbf{L} = \frac{\partial \mathbf{v}}{\partial \mathbf{x}}$. A superscript 1 denotes a macroscale measure. \mathbf{x} is the position and \mathbf{v} is the velocity within an RVE. \mathbf{n} is the unit normal to the surface S which encloses the RVE. $\boldsymbol{\sigma}$ and \mathbf{L} are the real stress and deformation rate fields over the RVE volume, V_{RVE} .

The homogenized internal power density is then given by

$$p_{\text{int}}(\mathbf{x}) = \bar{\boldsymbol{\sigma}}^1 : \bar{\mathbf{L}}^1. \quad (3)$$

The limitations of this continuum approach have been discussed above.

In the multiresolution formulation, we zoom into the macroscale RVE and examine the average behavior over a smaller microscale region known as the microaveraging domain, Ω^2 (superscript 2 denotes the microscale). The microaveraging domain encompasses the volume associated with a population of microstructural features which are characteristic of that scale, like that shown in Fig. 4 for a material containing microscopic spherical particles. The internal power density at a point \mathbf{x} is a combination of the contribution from the *macrodeformation rate*, $\bar{\mathbf{L}}^1$, and the difference $(\mathbf{L} - \bar{\mathbf{L}}^1)$, which represents the microscale contribution:

$$p_{\text{int}}(\mathbf{x}) = \bar{\boldsymbol{\sigma}}^1 : \bar{\mathbf{L}}^1 + \boldsymbol{\sigma}^2 : (\mathbf{L} - \bar{\mathbf{L}}^1), \quad (4)$$

where $\boldsymbol{\sigma}^2$ is introduced as the power conjugate stress measure of $(\mathbf{L} - \bar{\mathbf{L}}^1)$. The difference, $(\mathbf{L} - \bar{\mathbf{L}}^1)$, arises due to the non-uniform deformation field resulting from the microstructural heterogeneity. In Eq. (4) the microscale contribution to the internal power, $\boldsymbol{\sigma}^2 : (\mathbf{L} - \bar{\mathbf{L}}^1)$, is a local measure. It fails to capture the variation in the deformation which is related to the microscale interactions and consequently the microscale phenomena which determine the overall material properties.

By averaging over a surrounding volume [14], a non-local expression for the internal power density can be gained. The size of the averaging domain, Ω^z , is equal to the range of interactions at scale z . The range decreases with decreasing length scales. Here, we are concerned with a two-scale material only. The microaveraging domain, Ω^2 , centered on \mathbf{x} captures the microscale interactions which manifest themselves as variations in the deformation rate. The average behavior over Ω^2 defines the microscale material response. The power contribution from the *macrodeformation* is inherently a local measure i.e. macroscale interactions do not exist. The non-local internal power density becomes

$$p_{\text{int}}(\mathbf{x}) = \bar{\boldsymbol{\sigma}}^1 : \bar{\mathbf{L}}^1 + \int_{\Omega^2} \boldsymbol{\sigma}^2 : (\mathbf{L} - \bar{\mathbf{L}}^1) d\Omega. \quad (5)$$

For simplicity, the variation of \mathbf{L} is approximated as linear within the microaveraging domain, Ω^2 . Ω^2 is chosen to be small enough to validate such an assumption, yet large enough to ensure a variation of \mathbf{L} is still captured. A higher order approximation could be used, but would substantially complicate the model. The variation of the deformation rate, \mathbf{L} , within the micro averaging domain, Ω^2 , is written:

$$\mathbf{L}(\mathbf{x} + \mathbf{y}) = \bar{\mathbf{L}}^2 + (\bar{\nabla} \bar{\mathbf{L}}^2) \cdot \mathbf{y}, \quad (6)$$

where an over-bar, $\bar{\quad}$, represents an average over the corresponding averaging domain at that scale. Hence $\bar{\mathbf{L}}^2$ is the average deformation rate over the microaveraging domain, Ω^2 , or the *microdeformation rate*. $\bar{\nabla} \bar{\mathbf{L}}^2$ is the average of the gradient of

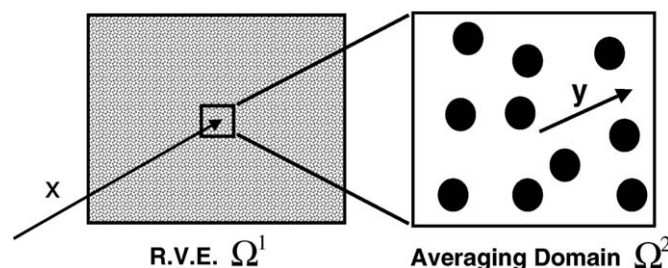


Fig. 4. The microaveraging domain Ω^2 lies within the RVE. It is representative of the microscale behavior.

the deformation over the microaveraging domain, Ω^2 , or the *microdeformation rate* gradient. Combining Eqs. (5) and (6), the two-scale internal power density is finally given by

$$p_{\text{int}}(\mathbf{x}) = \bar{\boldsymbol{\sigma}}^1 : \bar{\mathbf{L}}^1 + \bar{\boldsymbol{\sigma}}^2 : (\bar{\mathbf{L}}^2 - \bar{\mathbf{L}}^1) + \bar{\boldsymbol{\sigma}}^2 : (\bar{\nabla} \bar{\mathbf{L}}^2), \quad (7)$$

where $\bar{\boldsymbol{\sigma}}^2$ is called the *microstress* defined by the average of $\boldsymbol{\sigma}^2$ over the microaveraging domain and $\bar{\boldsymbol{\sigma}}^2$ is the *higher order microstress*, defined as the average of $\boldsymbol{\sigma}^2 \cdot \mathbf{y}$ over the micro averaging domain. The two-scale form for the internal power (Eq. (7)) has been derived before through a different approach by Cosserat [44]. This multiresolution homogenized internal power includes contributions from the *macrodeformation rate*, $\bar{\mathbf{L}}^1$, the *relative microdeformation rate*, $\bar{\mathbf{L}}^2 - \bar{\mathbf{L}}^1$, and the *microdeformation rate* gradient, $\bar{\nabla} \bar{\mathbf{L}}^2$. The microscale contributions account for the extra power associated with any localization effects due to microstructural heterogeneity and microscale interactions.

The multiresolution external power, kinetic power and governing equations have been developed and generalized to N scales of interest [15]. The virtual internal and external powers and the generalized stresses and deformation rates are given here:

$$\delta P_{\text{int}} = \int_{\Omega} \left\{ \bar{\boldsymbol{\sigma}}^1 : \delta \bar{\mathbf{L}}^1 + \sum_{\alpha=2}^N (\bar{\boldsymbol{\sigma}}^{\alpha} : (\delta \bar{\mathbf{L}}^{\alpha} - \delta \bar{\mathbf{L}}^1) + \bar{\boldsymbol{\sigma}}^{\alpha} : \delta \bar{\nabla} \bar{\mathbf{L}}^{\alpha}) \right\} d\Omega, \quad (8)$$

$$\delta P_{\text{ext}} = \int_{\Omega} \left\{ \mathbf{b}^1 \cdot \delta \mathbf{v}^1 + \sum_{\alpha=2}^N \mathbf{B}^{\alpha} : \delta \bar{\mathbf{L}}^{\alpha} \right\} d\Omega + \int_{\Gamma} \left\{ \mathbf{t}^1 \cdot \delta \mathbf{v}^1 + \sum_{\alpha=2}^N \mathbf{T}^{\alpha} : \delta \bar{\mathbf{L}}^{\alpha} \right\} d\Gamma, \quad (9)$$

$$\delta P = \delta P_{\text{int}} - \delta P_{\text{ext}} = 0. \quad (10)$$

The generalized stress and deformation measures can be defined as

$$\begin{aligned} \boldsymbol{\Sigma} &= [\bar{\boldsymbol{\sigma}}^1, \bar{\boldsymbol{\sigma}}^2, \bar{\boldsymbol{\sigma}}^2, \bar{\boldsymbol{\sigma}}^3, \bar{\boldsymbol{\sigma}}^3, \dots, \bar{\boldsymbol{\sigma}}^N, \bar{\boldsymbol{\sigma}}^N], \\ \boldsymbol{\Upsilon} &= [\bar{\mathbf{L}}^1, (\bar{\mathbf{L}}^2 - \bar{\mathbf{L}}^1), \bar{\nabla} \bar{\mathbf{L}}^2, (\bar{\mathbf{L}}^3 - \bar{\mathbf{L}}^1), \bar{\nabla} \bar{\mathbf{L}}^3, \dots, (\bar{\mathbf{L}}^N - \bar{\mathbf{L}}^1), \bar{\nabla} \bar{\mathbf{L}}^N]. \end{aligned} \quad (11)$$

In voigt notation, Eq. (8) can be written simply as

$$\delta P_{\text{int}} = \boldsymbol{\Sigma} \cdot \delta \boldsymbol{\Upsilon}. \quad (12)$$

where \mathbf{b}^1 and \mathbf{t}^1 are the body and traction forces respectively. \mathbf{B}^{α} and \mathbf{T}^{α} are the body and traction *double* forces respectively. For finite element implementation, the principal of virtual power is applied and discretized in the standard way. The generalized stress, $\boldsymbol{\Sigma}$, and generalized deformation rate, $\boldsymbol{\Upsilon}$, tensors replace the standard stress and strain tensors. Hence the multiresolution approach can be implemented in a standard finite element code with increased degrees of freedom.

2.2. Multiresolution constitutive relationships

In a multiresolution finite element analysis, a *generalized* constitutive relation is required to relate the generalized stress, $\boldsymbol{\Sigma}$, to the generalized deformation rate, $\boldsymbol{\Upsilon}$. The first step is to derive individual constitutive relationships at each scale by examining the micromechanics at each scale. The individual constitutive relationships, Φ^{α} , at each scale, α , can then be combined to create a *generalized* constitutive relation, Φ , as shown in Fig. 5. The generalized relationship is in rate form as

$$\dot{\boldsymbol{\Sigma}} = \mathbf{C}^{\text{ep}} : \boldsymbol{\Upsilon}, \quad (13)$$

where \mathbf{C}^{ep} is a general elastic–plastic tangent modulus.

Analytical derivation of a *generalized* constitutive relation, and hence determination of \mathbf{C}^{ep} , may be possible if the mechanics are simple and well understood. This approach is demonstrated for a polycrystalline material (Section 3.1) and a granular material (Section 3.2). For more complex problems involving more than two scales, a multiresolution *cell modeling* approach can be used. In a manner similar to the hierarchical approach, a constitutive relationship can be determined at the lowest scale of interest first. This relationship is used as an input when finding the constitutive behavior at the next largest scale and so on. The average behavior at scale α is determined by examining the average response over the averaging domain, Ω^{α} . At the macroscale, the averaging domain, Ω^1 , is simply the RVE. A generalized constitutive law is then formed based on the scale-specific behavior. This technique is used in the third example (Section 3.3) where crack propagation behavior in a porous material is investigated. It is also illustrated in more detail in the fourth example where an alloy containing particles at two scales is examined (Section 3.4). The final example illustrates a potential use of the

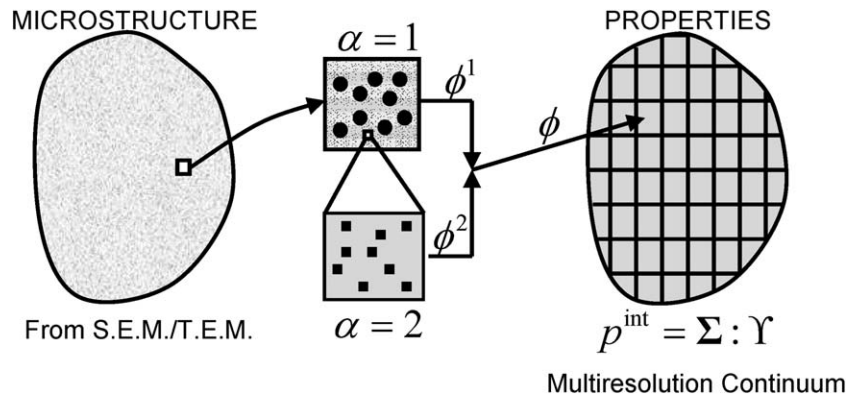


Fig. 5. Multiresolution homogenization approach. The constitutive behavior at each scale of interest is found. A generalized constitutive law can then be formed.

theory in the design of a theoretical bio-inspired self-healing material containing shape memory alloy inclusions (Section 3.5).

One benefit of forming a generalized constitutive relation is that it can be treated in a similar manner to a macroscale constitutive relation during numerical analysis. In Sections 3.3 and 3.4 a generalized Gurson type material law is used in a multiresolution finite element analysis. The stress and deformation invariants are simply replaced by *generalized* stress and deformation invariant measures where appropriate. The constitutive relation is then integrated using a fully implicit Newton return stress update algorithm.

3. Applications

The general nature of the outlined multiresolution approach ensures its viability for various types of materials. The approach is viable for any material which exhibits different constitutive behavior at different length scales. This generally infers that a discrete set of interacting entities exist at each scale of interest.

3.1. Dislocation hardening

3.1.1. Scale of dislocations

In crystalline materials such as metal alloys, plastic deformation is facilitated by dislocation movement along atomic slip planes. Work or strain hardening occurs when dislocation density increases to such an extent that dislocations begin to impede each other. It is known that the hardening behavior of materials is inherently a length scale dependent phenomena. Fleck et al. [16] showed that shear strength increases by a factor of 3 when twisting copper wires of size 12 μm compared to 170 μm . No change occurred in tension tests. Similar results are reported by Stolken and Evans [17] for bending of thin beams and by Nix [18] for micro and nanoindentation tests.

The hardening behavior can be related to the dislocation density through the well known Taylor relation:

$$\tau = \alpha\mu b\sqrt{\rho_s + \rho_G}, \quad (14)$$

where τ is the shear strength, μ is the shear modulus, b is the size of the Burger's vector, α is a constant of order unity, ρ_s is the density of statistically stored dislocations (SSD) and ρ_G is the density of geometrically necessary dislocations (GND). Statistically stored dislocations arise when a material is deformed in a homogeneous fashion. They are related to the level of plastic deformation within a sample.

GND density is directly related to the lattice curvature resulting from a heterogeneous deformation. Lattice curvature increases at smaller scales leading to high values of GND density. In other words, GND density increases as the length scale decreases, and becomes responsible for a significant amount of extra hardening, typically at scales below 10 μm which explains the experimental observations noted above.

As the name suggests, statistically stored dislocations (SSD) are a result of an average homogeneous deformation. SSD hardening is related to the average macroscale deformation and as such this is considered to be a macroscale phenomenon. GND induced hardening is prominent when higher gradients associated with heterogeneous microscale deformation exist. Conventional continuum models take no account of this small-scale gradient effect and become unrealistic at small scales. A crystalline material containing an SSD density and a GND density can be resolved at two scales as shown in Fig. 6. The effect of the SSD density can be captured by a distribution over the RVE. The geometrically necessary dislocations are

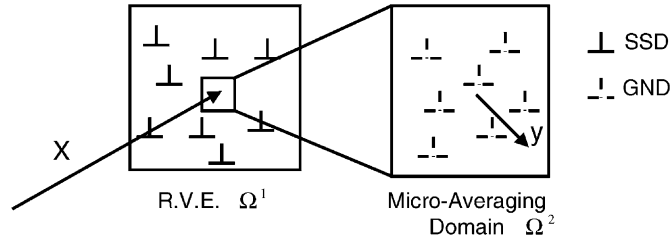


Fig. 6. SSD within the RVE. The microaveraging domain contains a population of geometrically necessary dislocations.

essentially a microscale feature. As such, the microaveraging domain contains a population of geometrically necessary dislocations.

In terms of *strain*, from Eq. (8), when $N = 2$ we find the internal energy density

$$w^{\text{int}}(\mathbf{x}) = \bar{\boldsymbol{\sigma}}^1 : \bar{\boldsymbol{\varepsilon}}^1 + \bar{\boldsymbol{\sigma}}^2 : (\bar{\boldsymbol{\varepsilon}}^2 - \bar{\boldsymbol{\varepsilon}}^1) + \bar{\boldsymbol{\sigma}}^2 : \nabla \bar{\boldsymbol{\varepsilon}}^2. \quad (15)$$

Geometrically necessary dislocations arise due to a microstrain *gradient* and not the strain itself. The only constraint on the system is that the microaveraging domain must capture a gradient in the deformation. In this case the microaveraging domain, Ω^2 , can be chosen as equal to the RVE. Now the macrostrain, $\bar{\boldsymbol{\varepsilon}}^1$, is equal to the average microstrain, $\bar{\boldsymbol{\varepsilon}}^2$. The internal energy density becomes

$$w^{\text{int}}(\mathbf{x}) = \bar{\boldsymbol{\sigma}}^1 : \bar{\boldsymbol{\varepsilon}}^1 + \bar{\boldsymbol{\sigma}}^1 : \bar{\boldsymbol{\eta}}^1, \quad (16)$$

where $\bar{\boldsymbol{\sigma}}^1$ is a higher order stress tensor such as that employed by Fleck and Hutchinson [19]. $\bar{\boldsymbol{\eta}}^1$ is the average strain gradient over the RVE, Ω^1 . To find the material behavior, we seek an analytical relationship between the stress and deformation fields within the RVE. This is then averaged over the microaveraging domain, Ω^2 , which coincides with the RVE, Ω^1 , in this case.

3.1.2. Flow stress

Consider the actual deformation fields within the RVE. It is common to relate the flow stress, σ , of a crystalline material to the shear strength, τ , as $\sigma = \sqrt{3}\tau$. From Eq. (14), the flow stress is given as

$$\sigma = \sqrt{3}\alpha\mu b\sqrt{\rho_s + \rho_G}. \quad (17)$$

A power law is commonly used to describe hardening associated with the SSD density:

$$\sigma = \sigma_{\text{ref}}(\varepsilon_{\text{eff}})^n, \quad (18)$$

where n is a hardening exponent, ε_{eff} is an effective strain given by $\sqrt{\frac{2}{3}}\boldsymbol{\varepsilon} : \boldsymbol{\varepsilon}$ and σ_{ref} is a reference yield stress. The GND density is related to the strain gradient, $\boldsymbol{\eta}$, and the Burger's vector size, b :

$$\rho_G = \frac{\eta_{\text{eff}}}{b}, \quad (19)$$

where η_{eff} is an effective value of the strain gradient given by Gao et al. [20] as $\sqrt{\frac{1}{4}}\boldsymbol{\eta} : \boldsymbol{\eta}$. Subsequently, Gao et al. modified the flow stress of Eq. (18) to incorporate the effects of the GND density:

$$\sigma = \sigma_{\text{ref}}\sqrt{(\varepsilon_{\text{eff}})^{2n} + l\eta_{\text{eff}}} \quad (20)$$

l is an internal length which is necessary for dimensional consistency. Comparing Eq. (20) to (17), an expression for l is found in terms of the material parameters:

$$l = 3\alpha^2\left(\frac{\mu}{\sigma_{\text{ref}}}\right)^2 b. \quad (21)$$

The length, l , conveys information relating to the hardening effect of GND density. When the deformation is on the order of this length scale, significant hardening occurs due to the effect of geometrically necessary dislocations.

3.1.3. Yield criterion

The internal energy density at a point in the RVE can be written as

$$w^{\text{int}} = \boldsymbol{\sigma} : \boldsymbol{\varepsilon}, \quad (22)$$

where $\boldsymbol{\sigma}$ and $\boldsymbol{\varepsilon}$ are again the actual stress and strain fields within the RVE. The yield criterion is now formulated in terms of the equivalent form of the stress, σ_{eq} , and the flow stress, σ :

$$\sigma_{\text{eq}} = \sigma \text{ or } \sigma_{\text{eq}} = \sigma_{\text{ref}} \sqrt{(\varepsilon_{\text{eff}})^{2n} + l\eta_{\text{eff}}}. \quad (23)$$

For associate plasticity the deviatoric part ($\boldsymbol{\zeta}$) of the stress $\boldsymbol{\sigma}$, can be related to the equivalent stress, σ_{eq} :

$$\boldsymbol{\zeta} = \frac{2\sigma_{\text{eq}}}{3\varepsilon_{\text{eff}}} \boldsymbol{\varepsilon}. \quad (24)$$

As we are considering plastic deformation only, $\boldsymbol{\varepsilon}$ is a deviatoric measure. This is an expression for the local stress field within the RVE in terms of the plastic strain and strain gradient. As before, only the first order variation in the strain field is considered in the microaveraging domain, which is the RVE in this case:

$$\boldsymbol{\varepsilon}(\mathbf{y}) = \bar{\boldsymbol{\varepsilon}}^1 + \bar{\boldsymbol{\eta}}^1 \cdot \mathbf{y}, \quad (25)$$

where $\bar{\boldsymbol{\varepsilon}}^1$ is the average of the strain, $\boldsymbol{\varepsilon}$, over the RVE and $\bar{\boldsymbol{\eta}}^1$ is the average of the strain gradient, $\boldsymbol{\eta}$, over the microaveraging domain (which coincides with the RVE in this case).

3.1.4. Two scale constitutive relation

It is now possible to extract the constitutive relation by averaging the stress over the RVE. These quantities are deviatoric as they are a result of isochoric plastic deformation.

$$\bar{\boldsymbol{\zeta}}^1 = \frac{1}{V_{\Omega^1}} \int_{\Omega^1} \boldsymbol{\sigma} dV, \quad (26)$$

where $\bar{\boldsymbol{\zeta}}^1$ is the deviatoric part of the *macrostress* $\bar{\boldsymbol{\sigma}}^1$ and where $\boldsymbol{\sigma}$ is given by Eqs. (23)–(25). The higher order stress, $\bar{\boldsymbol{\sigma}}^1$, is determined by averaging the first moment of the stress over the microaveraging domain (Ω^2), which coincides with the RVE (Ω^1) here:

$$\bar{\boldsymbol{\sigma}}^1 = \frac{1}{V_{\Omega^1}} \int_{\Omega^1} \mathbf{y} \cdot \boldsymbol{\sigma} dV \quad (27)$$

Eqs. (26) and (27) describe the material constitutive behavior in terms of effective measures of the average strain and average gradient of the strain over an RVE. The length scale of the RVE is implicitly embedded in the two scale constitutive relation through this averaging procedure. The size of the RVE is chosen to be on the order of l i.e. a square shaped RVE in 2 dimensions will have a side of length l . As an example, l is given as 2.8 μm by Chen and Wang [21] for copper. Deformation fields with a gradient, $\bar{\boldsymbol{\eta}}^1$, on the order of l will increase the level of hardening due to geometrically stored dislocations. The multiresolution approach captures the important gradient effects at small length scales. It decomposes to, and is consistent with, the higher order strain gradient plasticity theory of Fleck and Hutchinson [19].

3.2. Granular material

A granular material is a large assembly of discrete solid grains such as sand, gravel, coal, pharmaceutical pills, coffee beans, corn and animal feed. Although the behavior of individual grains is quite simple, the overall system behavior is complex. The importance of understanding granular materials lies in their usage in industrial processes and their disastrous effects in natural phenomena such as land slides. Energy dissipation and momentum transfer is complicated as it occurs due to direct interaction between neighboring grains. Hence, the flow characteristics of such materials are directly related to the granular architecture. A general approach to modeling granular flow still does not exist. Industrially, increased understanding of granular materials has the potential to save millions of dollars [22].

Here we consider a material consisting of microscale spherical grains, modeled as discs in a two dimensional analysis. This problem has been studied in a multiresolution context by Kadowaki and Liu [23,45]. It has been chosen to demonstrate the applicability of the outlined method to a material which clearly demonstrates a microscale deformation mechanism very much distinct from the macroscale behavior. The microaveraging domain therefore contains a population of grains at the microscale (Fig. 7). On an individual basis, each grain can be considered incompressible. Under compressive loading, deformation occurs due to slippage along granular slip planes. The average macroscale deformation can be attributed to this slippage effect. At the microscale, relative movement between grain surfaces results in grain rotation and frictional energy dissipation. Microscale deformation is therefore a result of rotational slip between neighboring grains.

At both scales in compression, a small elastic deformation is followed by a plastic regime. As the grains are restricted to rigid body rotations, only the antisymmetric part (\mathbf{W}) of the deformation rate, \mathbf{L} , is considered at the microscale. According to Eq. (8) when $N = 2$, the internal power density becomes

$$p_{\text{int}}(\mathbf{x}) = \bar{\boldsymbol{\sigma}}^1 : \bar{\mathbf{L}}^1 + \bar{\boldsymbol{\sigma}}^2 : (\bar{\mathbf{W}}^2 - \bar{\mathbf{W}}^1) + \bar{\boldsymbol{\sigma}}^3 : (\bar{\nabla} \bar{\mathbf{W}}^2). \quad (28)$$

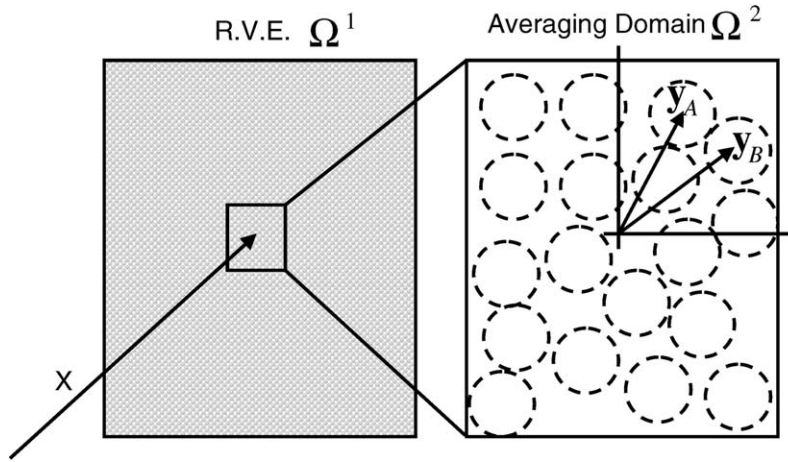


Fig. 7. RVE and microaveraging domain. The averaging domain captures a linear variation in the microstrain across a population of grains.

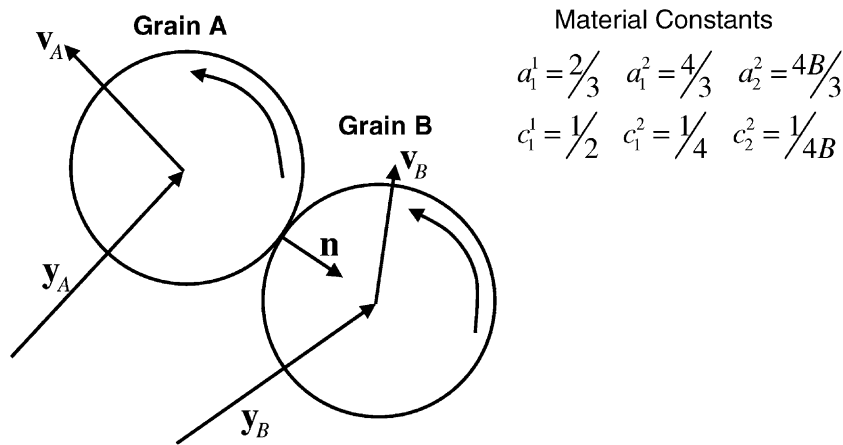


Fig. 8. Grain A and B within the averaging domain. Contact occurs at the touching surface. A slip measure can be defined in terms of the relative velocity at the contact point.

3.2.1. Elastic regime

Here we deal with the elastic part of the deformations, denoted by subscript e. The macroscale elastic behavior can be determined by averaging the flow response over the RVE. The microscale behavior is found by averaging the flow behavior over the microaveraging domain, Ω² (Fig. 8). The macroscale constitutive response is simply

$$\dot{\sigma}^1 = \mu^1 : \bar{\mathbf{L}}_e^1, \tag{29}$$

where μ¹ is the macroscopic elastic modulus. The simplest way to describe the elastic behavior within the microaveraging domain is:

$$\dot{\sigma}^2 = \mu^2 : (\mathbf{W}_e - \bar{\mathbf{W}}_e^1), \tag{30}$$

where μ² is the microscale elastic rotation modulus. The microscale elastic behavior is found by averaging this behavior over the microaveraging domain, Ω² (Fig. 7):

$$\dot{\sigma}^2 = \mu^2 : (\bar{\mathbf{W}}_e^2 - \bar{\mathbf{W}}_e^1). \tag{31}$$

In the microaveraging domain, the first moment of the microstress is given by

$$\dot{\sigma}^2 \bullet \mathbf{y} = \mu^2 : (\mathbf{W} - \bar{\mathbf{W}}_e^1) \bullet \mathbf{y}, \tag{32}$$

where \mathbf{y} is the position relative to the center of the averaging domain (Fig. 8). Again we assume a linear variation of the deformation \mathbf{W}_e , within the microaveraging domain. Averaging Eq. (32) over the microaveraging domain, the higher order microstress measure, $\overline{\overline{\boldsymbol{\sigma}^2}}$ can be related to the average gradient ($\overline{\nabla \mathbf{W}_e^2}$) of the *microdeformation rate*:

$$\overline{\overline{\boldsymbol{\sigma}^2}} = \boldsymbol{\mu}^2 : \mathbf{B} \bullet (\overline{\nabla \mathbf{W}_e^2}), \quad (33)$$

where $\mathbf{B} = \frac{1}{V_{\Omega^2}} \int_{\Omega^2} \mathbf{y} \otimes \mathbf{y} \, d\Omega$.

The elastic behavior is fully described.

3.2.2. Plastic regime

Here we deal with the plastic part of the deformations, denoted by subscript p. Plastic deformation at both scales occurs due to slippage in a similar way to dislocation plasticity in metals. Therefore, a Mises type yield surface is appropriate. An extension of the J_2 flow theory of plasticity to two scales can be made. The flow rule becomes

$$\Phi = \frac{\sqrt{3\tilde{J}_2}}{\Sigma_Y(\mathcal{I}_{\text{eff}})} - 1 = 0. \quad (34)$$

The two-scale form of the second stress invariant, \tilde{J}_2 , can be written in terms of the stress measures as

$$\tilde{J}_2 = a_1^1 \bar{\boldsymbol{\zeta}}^1 : \bar{\boldsymbol{\zeta}}^1 + a_1^2 \bar{\boldsymbol{\sigma}}^2 : \bar{\boldsymbol{\sigma}}^2 + \frac{a_2^2}{(l^2)^2} \overline{\overline{\boldsymbol{\sigma}^2}} : \overline{\overline{\boldsymbol{\sigma}^2}}, \quad (35)$$

where $\bar{\boldsymbol{\zeta}}^1$ is the deviatoric part of the macrostress, $\bar{\boldsymbol{\sigma}}^1$, and l^2 is the characteristic size of the microaveraging domain introduced for dimensional consistency. For a square averaging domain in two dimensions, $A_{\Omega^2} = l^2 \times l^2$, where A_{Ω^2} is the area of the microaveraging domain, Ω^2 . The generalized yield stress, Σ_Y , is a function of the two-scale version of the effective plastic strain, $\dot{\mathcal{I}}_{\text{eff}}$:

$$\dot{\mathcal{I}}_{\text{eff}} = \sqrt{c_1^1 \bar{\mathbf{L}}_p^1 : \bar{\mathbf{L}}_p^1 + c_1^2 (\overline{\mathbf{W}}_p^2 - \overline{\mathbf{W}}_p^1) : (\overline{\mathbf{W}}_p^2 - \overline{\mathbf{W}}_p^1) + c_2^2 (l^2)^2 (\overline{\nabla \mathbf{W}}_p^2) : (\overline{\nabla \mathbf{W}}_p^2)}. \quad (36)$$

Eqs. (35) and (36) contain several unknown constants. In each constant the superscript represents the scale of the associated tensor and the subscript describes its order. For example a_2^2 is associated with the microscale (superscript 2) and a higher order tensor (subscript 2). This convention is used throughout. The unknown material constants are determined by examining the distinct material behavior at each scale. At the macroscale, conventional J_2 theory can well describe the behavior due to the slip mechanism of deformation. At the microscale, the interactions between neighboring grains become an important factor. A rotating grain will exert a frictional force on all other neighboring grains, transmitted through the grain surfaces. The effect of one rotating grain will propagate through the material and eventually dissipate. The range of this interaction is physically related the length scale of a grain.

With reference to Fig. 8, a measure of slip can be defined at the contact point, associated with direction \mathbf{n} . This describes the relative motion between two neighboring grains:

$$s_c^2(\bar{\mathbf{L}}_p^1, \mathbf{W}_p) = \frac{1}{(2\pi R)^2} \Delta \mathbf{v}_c^t : \Delta \mathbf{v}_c^t, \quad (37)$$

where R is the grain radius and $\Delta \mathbf{v}_c^t$ is the tangential component of the relative velocity at the contact point. $\Delta \mathbf{v}_c^t$ can easily be found in terms of the macro and microdeformation rates at the contact point and the grain radius, R :

$$\Delta \mathbf{v}_c^t = 2R(\bar{\mathbf{L}}_p^1 \bullet \mathbf{n} - \mathbf{W}_p \bullet \mathbf{n} - \mathbf{n} \bullet \bar{\mathbf{L}}_p^1 \bullet \mathbf{n} \otimes \mathbf{n}). \quad (38)$$

The total slip over all directions, \tilde{s}^2 , is given by [23]:

$$\tilde{s}^2 = \int_0^{2\pi} s_c^2 \, d\theta. \quad (39)$$

The square of the rate of effective plastic strain, $\dot{\mathcal{I}}_{\text{eff}}$, is proportional to the average of this measure over the microaveraging domain, Ω^2 [23].

$$(\dot{\mathcal{I}}_{\text{eff}})^2 = \frac{C_1}{V_{\Omega^2}} \int_{\Omega^2} \tilde{s}^2 \, d\Omega. \quad (40)$$

To enable an analytical treatment, the size of the microaveraging domain is chosen to be $10R$. This is the typical range of interaction between grains observed experimentally. After some algebra, Eq. (40) produces the constants a_1^1 , a_1^2 and a_2^2 . Following the J_2 flow theory to its conclusion, the condition that the plastic rate parameter, $\dot{\lambda}$, is equal to the effective plastic strain rate, $\dot{\mathcal{I}}_{\text{eff}}$, yields the unknown constants b_1^1 , b_1^2 and b_2^2 within the two-scale stress invariant, \tilde{J}_2 . The constants are given in Fig. 8, where B is related to the dimensions of the averaging domain.

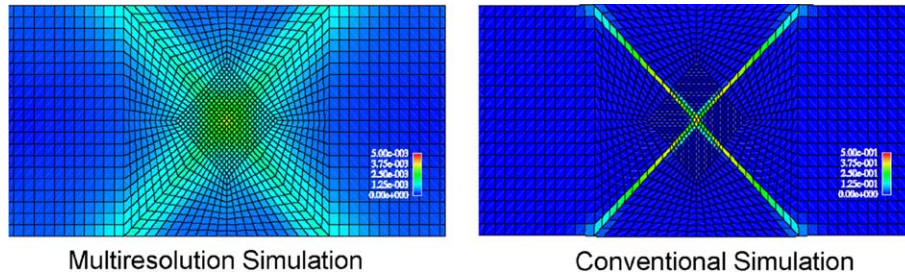


Fig. 9. Simulated contours of plastic strain in a granular material. Comparison of multiresolution and conventional approaches [23]. Realistic shear band behavior is found by using the multiresolution approach. The conventional approach suffers from the absence of a real length scale.

From a material design perspective, this proves to be a useful result because the material constants incorporate the length scale associated with the grain size. Granular flow initiates through the formation of shear bands caused by localized deformation fields. The prediction of the flow characteristics of granular materials can only be achieved by accurately simulating these shear bands. The simulations in Fig. 9, which show a granular material under compression, were performed using the bridging scale method [46,47]. In general, one performs a fine mesh computation only in a localized region of interest e.g. in a region containing a shear band; while a coarse-scale mesh is employed in the surrounding region. A fine-scale solution can be approximated by a coarse-scale solution overlaid by a fine-scale solution. By incorporating an impedance force, the fine mesh can be limited to the region of interest only. This method has been used previously by Wagner and Liu [48] to concurrently perform atomic-scale calculations and macroscale finite element calculations. Here, the bridging scale method is used as a convenient method for restricting the fine mesh to the region of interest which has obvious benefits in terms of computer simulation efficiency.

In Fig. 9, the conventional continuum approach does not take account of the microscale gradient effects which arise due to the granular interaction. The simulation gives mesh dependent results i.e. all of the deformation localizes in the elements within the localized region even when a very fine mesh is used. This is a common problem in continuum simulations which use softening behavior in the material law [24]. The multiresolution simulation predicts the shear band behavior much more realistically than a regular continuum model. This is possible because the model contains embedded information pertaining to the range of influence exerted by individual grains during microscopic localization. This range is linked to the characteristic length scale of the grains. The microscale constitutive relationship, which is prevalent at that scale, more accurately predicts the shear band behavior in the fine mesh based on the *microdeformation* and the *microdeformation* gradient. A realistic shear band width is predicted which is consistent with experimental findings [54].

3.3. Porous materials

In Section 3.2, for granular materials only the spin is important in terms of microscale deformation of grains. Consider now a material containing microscale voids such as a porous metal alloy. In such a material, microscale deformation is controlled by the growth of voids. Void growth is a volumetric process and as such is a function of the hydrostatic stress only. It is reasonable to assume that the volumetric part of the *microdeformation* plays a prominent role in the microscale deformation of such materials. The material can be decomposed as before into the macro and microscales as shown in Fig. 10.

With this in mind, according to Eq. (8), a porous metal's internal power can be written:

$$p_{\text{int}}(\mathbf{x}) = \bar{\boldsymbol{\sigma}}^1 : \bar{\mathbf{L}}^1 + \bar{\boldsymbol{\sigma}}^2 : (\bar{\mathbf{L}}_v^2 - \bar{\mathbf{L}}^1) + \bar{\boldsymbol{\sigma}}^2 : (\nabla \bar{\mathbf{L}}_v^2), \quad (41)$$

where subscript v represents the volumetric part of the deformation. A generalized constitutive relationship in the form of a Gurson model can be used to describe the plastic deformation of a porous material in the multiresolution framework. Void growth and softening are now functions of the macrostress, the microstress and the higher order microstress. The material constants present in this generalized Gurson model can be found computationally. By applying different boundary conditions to a microaveraging domain (Fig. 10), Ω^2 , the resulting average stress and void volume fraction in the averaging domain can be plotted. A curve consistent with the form of the Gurson potential can be overlaid on this data in a manner which allows the material constants to be extracted.

This method is used to study the behavior of a pre-cracked porous material through the finite element method, as shown in Fig. 11. The material in the vicinity of the crack is discretized with a very fine mesh to capture the strong deformation gradients in that region. The whole sample is simultaneously discretized with a coarse mesh. The two meshes are modeled concurrently using the Bridging Scale Method [46,47]. In Fig. 11 a tensile force is applied to the sample. The top and bottom surfaces are free and, as expected, a shear band initiates at the crack tip. Localization near the crack tip is simulated

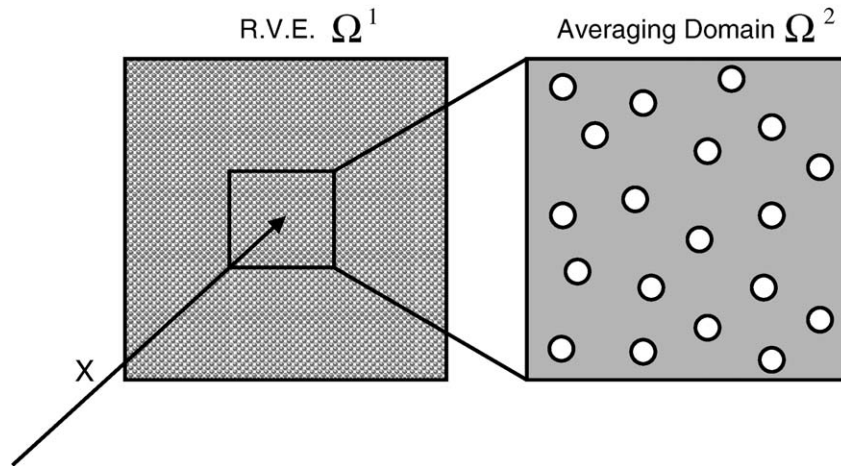


Fig. 10. A porous material can be resolved to two scales, the macroscale and microscale. A typical microaveraging domain includes several voids.

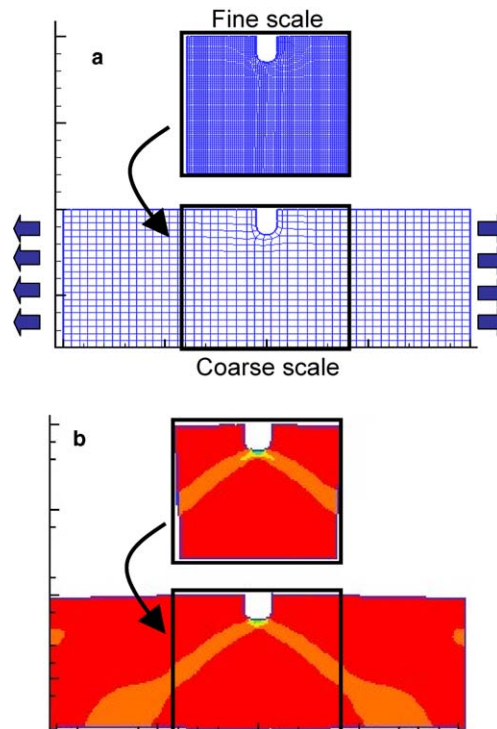


Fig. 11. Simulated plastic strain contours in a loaded sample. (a) The Bridging scale method is used to model a pre-cracked sample and (b) more severe localization is predicted in the fine mesh which captures the microscale deformation and softening due to void growth.

more accurately in the fine mesh which captures variations in the deformation on the order of the microscale i.e. the *microdeformation* rate and its gradient. This microdeformation results in increased softening and further localization due to void growth, according to the Gurson type material law used to describe the microscale constitutive behavior.

Fig. 12 is another simulation of a crack being opened under mode I loading. An important difference from Fig. 11 is that the bottom surface is constrained and the system approximates to a surface crack in a semi-infinite body. Again the Bridging Scale Method is employed as a means of capturing the small-scale deformation fields near the crack tip. The coarse-scale calculations do not capture the localized deformation and strong gradients near the crack tip. It is therefore impossible to simulate the crack propagation behavior accurately. By zooming into the finely meshed region (Fig. 12b) it is evident that the strong microscale gradients in this region are playing an important role in terms of crack propagation. These gradients give rise to much more void growth and softening than is predicted by the coarse-scale approximation. The fine-scale localization is on the order of the crack size and is consistent with the ductile fracture behavior observed experimentally in porous materials.

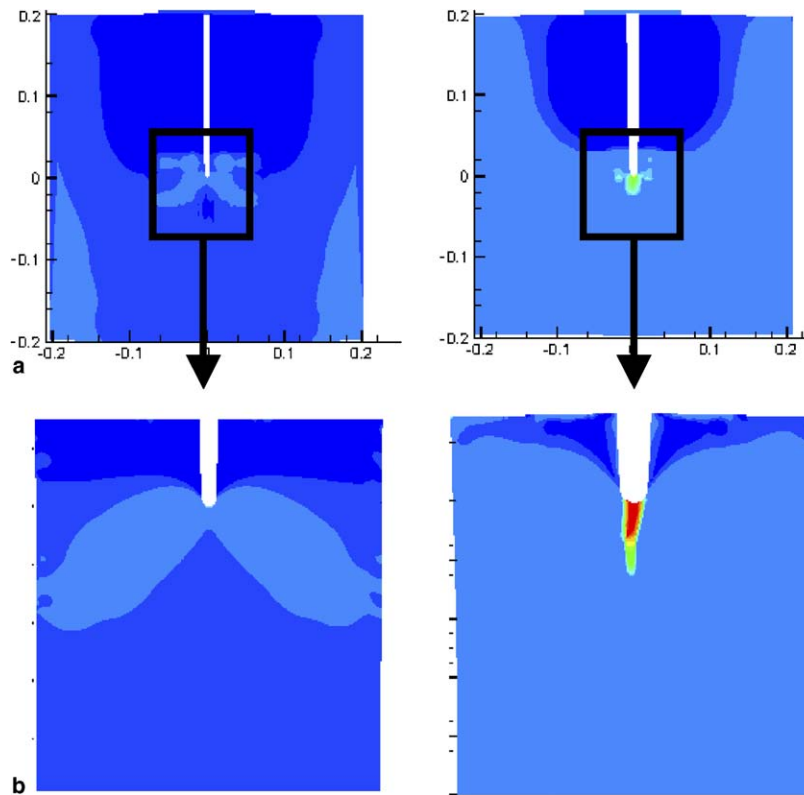


Fig. 12. Simulated plastic strain contours in a loaded sample. (a) A crack loaded in Mode I. The bottom surface is constrained; the system approximates to surface crack in an infinite body. (b) Crack propagation is predicted in the fine mesh which captures the microscale deformation and softening due to void growth.

3.4. Alloys

Very pure polycrystalline metals can sustain high levels of stable plastic flow due to the dislocation mechanism described in Section 3.1. Specimen failure is generally due to geometric instabilities. A tensile specimen of pure polycrystalline metal theoretically fails through extreme necking i.e. a 100% reduction in cross sectional area at the geometrical instability point. Although very tough, these metals are not strong enough for many engineering and structural applications. To improve strength, specific compounds or elements are added during processing. The final microstructure and properties of an alloy depend strongly on how these alloying additives behave during processing and subsequent heat treatments. Additives vary in thermal stability, solubility and reactivity with the surrounding metal matrix. Ultimately, they tend to either occupy interstitial atomic sites in the lattice or clump together and eventually precipitate out as particles of varying size and coherency with the matrix [49].

3.4.1. Strengthening mechanisms

Interstitial atoms do not fit well in the surrounding atomic lattice. This misfit leads to local strain fields which have the benefit of impeding dislocation movement, making plastic deformation more difficult. The process is known as coherency hardening. A more efficient strengthening method is realized by introducing strengthening particles. This involves the precipitation of particles composed of insoluble compounds formed by reaction of the additives with each other and with the metal matrix. In some alloys it is possible to perform heat treatments to induce the precipitation. For example, in heat treatable aluminium alloys a supersaturated solid solution can be formed by heating the alloy to a high temperature. The temperature is controlled to produce precipitates ranging from small coherent particles to large incoherent particles during the subsequent quenching process. In ultra high strength steels, titanium carbide particles are introduced for the same purpose.

In both cases, the particles impede dislocation movement and thereby increase strength. Their effectiveness depends on their size and coherency, as illustrated in Fig. 13. Interstitial atoms are generally a different size than surrounding atoms. The resulting misfit between the interstitial atom and the lattice gives rise to a localized strain field around the particle. Small strengthening particles are coherent with the surrounding matrix material. To facilitate the coherency at the particle–matrix interface, the surrounding material is subjected to a strain. In both cases, the surrounding strain field resists the

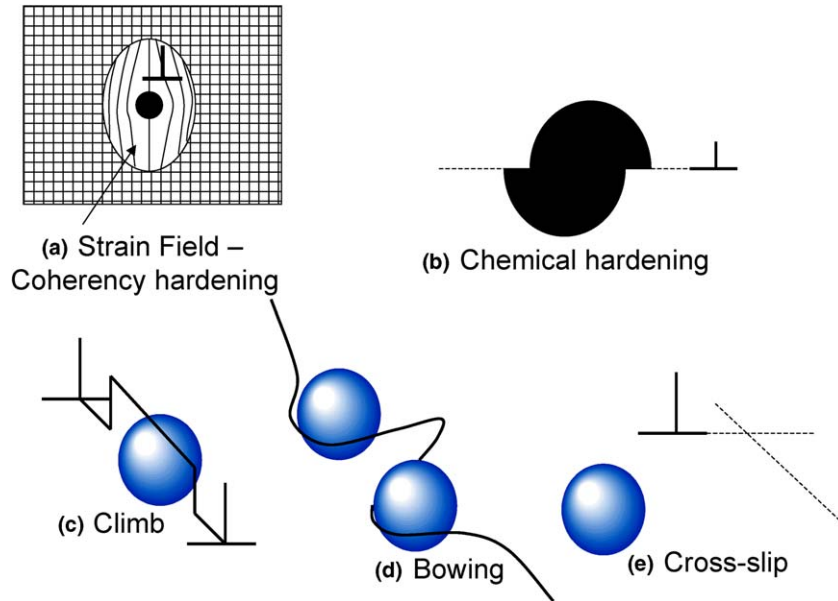


Fig. 13. Particle hardening mechanisms. (a) The strain field around interstitial atoms and small particles impedes dislocations. (b) Dislocations are forced to shear through mid-sized particles. Dislocations by-pass large particles by (c) climb, (d) bowing and (e) cross slip mechanisms.

movement of dislocations either by attracting them toward the strain field, which they then have difficulty escaping from, or by resisting the movement of dislocations toward the strain field (Fig. 13a).

Mid-sized particles remain coherent with the matrix and again a local strain field arises. However, the effect of the strain field is much less than the effect of the actual particle itself in terms of impeding dislocations. Because the particles are coherent and relatively large, dislocations must shear through them (chemical hardening). The particles are harder than the matrix material and extra work is required to move the dislocation through the particle; hence the dislocation is impeded. This form of particle strengthening is very effective (Fig. 13b).

Large particles are incoherent with the matrix material. As they are generally quite far apart, dislocations can bypass them by climbing onto another slip plane in the locality of the particle (Fig. 13c). Alternatively, a dislocation line can bow between two particles, forming dislocation loops around the particles before continuing on (Fig. 13d). The third mechanism, cross slip, involved the dislocation switching onto a different slip plane where it will not be confronted by the particle (Fig. 13e). Particles above a certain size provide very little resistance to dislocation movement as they are usually quite widely spaced; dislocations can easily bypass them by bowing through between them [49].

3.4.2. Ductile fracture behavior

Unfortunately, unwanted larger ‘inclusions’ (e.g. constituent particles in aluminum alloys and titanium nitrides in steel alloys) form as a by-product of the raw material processing. These particles are often too large to effectively impede dislocation movement and their only contribution is to aid ductile fracture.

The surface energy of an inclusion is given by

$$E = \gamma \cdot S, \quad (42)$$

where γ is the debonding energy per unit surface area and S is the surface area of the inclusion. For a spherical inclusion of radius R , the surface energy per volume is

$$\frac{E}{V} = \frac{3\gamma}{\pi R} \sim \frac{1}{R}, \quad (43)$$

where V is the inclusion volume. An inverse relationship exists between the surface energy per volume and the particle radius. The interfacial strength between the large inclusions and the surrounding matrix material is therefore generally quite low and debonding occurs at very small plastic strains [25]. Decohesion of the two surfaces can be thought of as a void nucleation mechanism. Under hydrostatic conditions, the two surfaces are pulled further apart and the voids grow. The process known as void coalescence begins when the stress field emanating from one void interacts with the stress field of another void [26], creating a localized field between the voids. At this point, the voids may continue to grow and physically impinge upon each other, propagating a crack (Fig. 14a).

Alternatively, the much smaller strengthening particles between voids may themselves debond from the matrix and nucleate microvoids due to the localization in that region (Fig. 14b). The microvoids grow and geometrically impinge upon

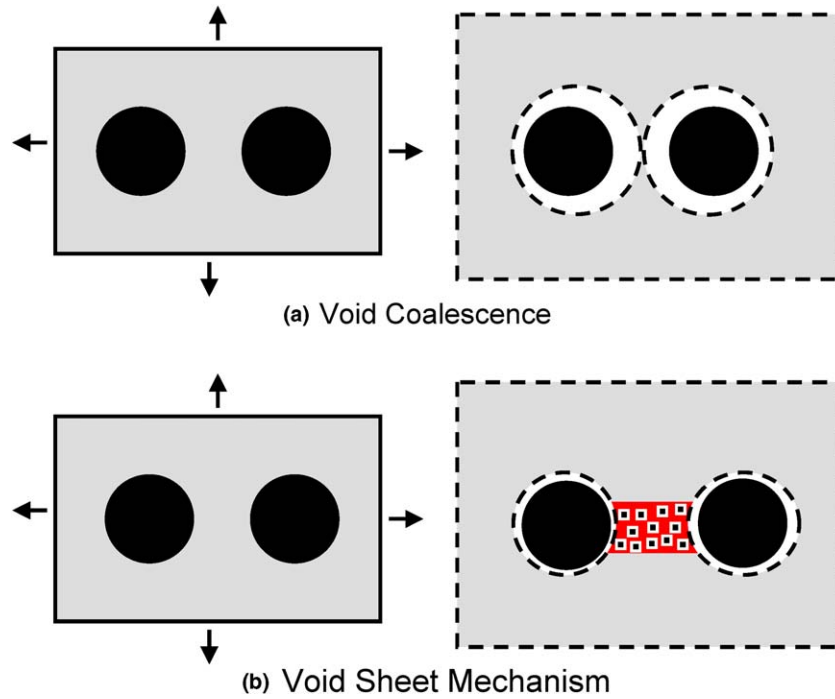


Fig. 14. Comparison of void coalescence and void sheet mechanism. (a) Voids physically impinge upon one another. (b) The localization between two large voids causes microvoid nucleation at the site of the much smaller strengthening particles.

each other on a plane between the large inclusions. This leads to internal micronecking of the matrix material between inclusions. This void sheet mechanism is common in alloys and is a perfect example of interaction between two distinct scales. Even under a pure shear load, the localized field will contain a hydrostatic component. So although the precipitated particles increase strength, they often contribute to ductile fracture. Consequently, fracture toughness is considerably reduced with an increasing amount of particles as was shown experimentally by Edelson and Baldwin [27].

Ductile fracture is triggered by interfacial decohesion of the inclusions and propagates through the smaller strengthening particles. This premature softening of the material has a negative effect on both the strength and toughness. A tensile specimen will fail well before reaching the level of necking possible in a pure polycrystalline metal. Hence, the introduction of precipitated particles is consistent with the inverse strength–toughness relationship common in material systems i.e. stronger materials have lower fracture toughness. The fundamental problem of alloy design is how to improve both strength and toughness, or at least *optimize* the microstructure to achieve a satisfactory level of both.

3.4.3. Multiresolution model

Such alloys can be resolved to three scales; the macroscale, the microscale containing inclusions (also known as primary particles) such as titanium nitrides in steel alloys and the sub-microscale containing strengthening particles (also known as secondary particles) such as titanium carbides in steel alloys. In aluminium alloys, the inclusion particles range in size from 1 to 30 μm and the strengthening particles range in size from 1 to 100 nm. In ultra high strength steels, the inclusions are usually larger than 1 μm and the strengthening particles are approximately 10–100 nm. In both cases, there is a factor of 10–100 in the difference between the microscale and subscale particle size.

The multifield internal power now incorporates the average deformation at each of the scales and the average gradient of the deformation at the micro ($\alpha = 1$) and submicroscale ($\alpha = 2$) (Fig. 15).

$$p_{\text{int}}(\mathbf{x}) = \bar{\boldsymbol{\sigma}}^1 : \bar{\mathbf{L}}^1 + \bar{\boldsymbol{\sigma}}^2 : (\bar{\mathbf{L}}^2 - \bar{\mathbf{L}}^1) + \bar{\boldsymbol{\sigma}}^2 : (\bar{\nabla} \bar{\mathbf{L}}^2) + \bar{\boldsymbol{\sigma}}^3 : (\bar{\mathbf{L}}^3 - \bar{\mathbf{L}}^1) + \bar{\boldsymbol{\sigma}}^3 : (\bar{\nabla} \bar{\mathbf{L}}^3). \quad (44)$$

The generalized stress now becomes

$$\boldsymbol{\Sigma} = [\bar{\boldsymbol{\sigma}}^1, \bar{\boldsymbol{\sigma}}^2, \bar{\boldsymbol{\sigma}}^2, \bar{\boldsymbol{\sigma}}^3, \bar{\boldsymbol{\sigma}}^3] \quad (45)$$

and the generalized strain becomes

$$\boldsymbol{\Upsilon} = [\bar{\mathbf{L}}^1, (\bar{\mathbf{L}}^2 - \bar{\mathbf{L}}^1), \bar{\nabla} \bar{\mathbf{L}}^2, (\bar{\mathbf{L}}^3 - \bar{\mathbf{L}}^1), \bar{\nabla} \bar{\mathbf{L}}^3]. \quad (46)$$

A generalized constitutive relation is required which relates $\boldsymbol{\Sigma}$ to $\boldsymbol{\Upsilon}$. Following Fig. 16, starting at the smallest scale and moving up, a constitutive relation can be derived at each scale. Once the behavior of each scale is known, a generalized

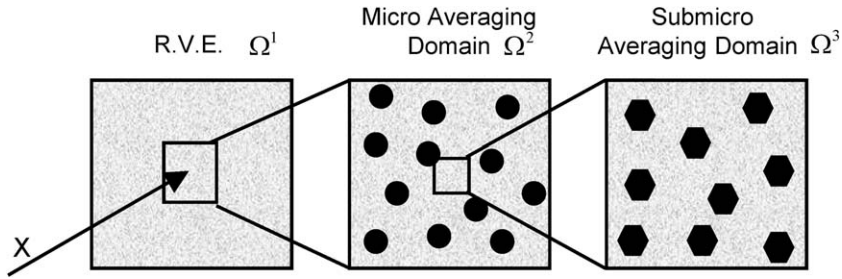


Fig. 15. Multiresolution decomposition of an alloy with two scales of particles. The larger inclusions are represented by circles. The microaveraging domain contains a population of inclusions. The submicroaveraging domain contains a population of strengthening particles represented by hexagons.

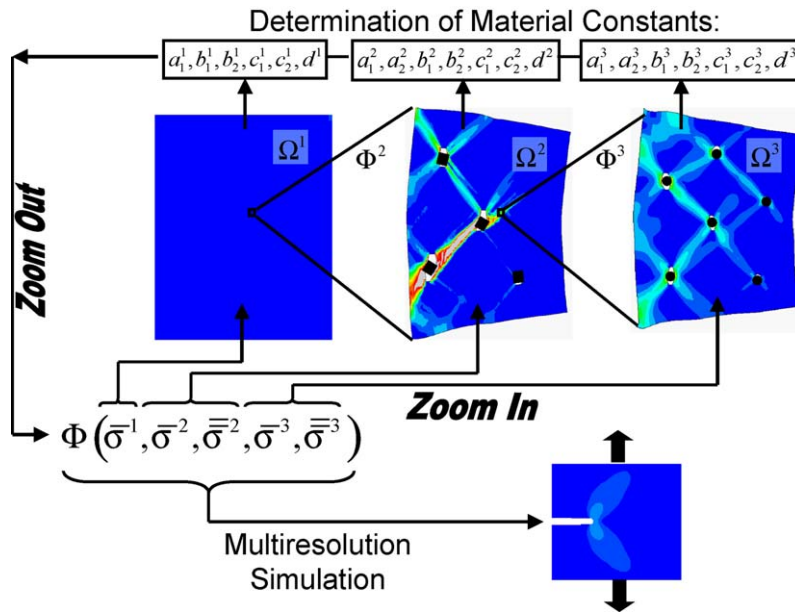


Fig. 16. Derivation of a multiscale constitutive law. The constitutive behavior is found at each scale through a hierarchical approach i.e. the homogenized behavior at one scale is used to represent the matrix behavior at the next largest scale. The constants in the generalized constitutive law can simultaneously be found at each scale.

constitutive relation can be formed. Again the behavior at each scale is first considered in the elastic regime. We consider the elastic behavior at each scale to be independent. The simplest way of representing the elastic response is through a generalized elastic relationship:

$$\begin{pmatrix} \dot{\sigma}^1 \\ \dot{\sigma}^2 \\ \dot{\sigma}^2 \\ \dot{\sigma}^3 \\ \dot{\sigma}^3 \end{pmatrix} = \begin{bmatrix} [C^1] & & & & \\ & [C^2] & & & \\ & & [B^2] & & \\ & & & [C^3] & \\ & & & & [B^3] \end{bmatrix} \begin{pmatrix} \bar{L}^1 \\ \bar{L}^2 - \bar{L}^1 \\ \nabla \bar{L}^2 \\ \bar{L}^3 - \bar{L}^1 \\ \nabla \bar{L}^3 \end{pmatrix}^e, \tag{47}$$

where the superscript e represents the elastic component.

The plastic yielding behavior of a material which contains particles can be described by a Gurson [11] like yield surface which accounts for the softening behavior due to void growth. An appropriate nucleation law is required to model the debonding behavior of the particles. A Gurson model can be employed to capture the average softening behavior associated with a particular scale due to the presence and growth of voids at that scale. Here, it is used separately to describe the material behavior at each individual scale. The generalized material behavior can then be described by a Gurson-like constitutive model extended to three scales:

$$\Phi(\Sigma, \gamma_{\text{eff}}, F) = \frac{3\tilde{J}_2}{\Sigma_y^2} + q_1 \frac{\Sigma_m}{\Sigma_y} + 2q_2 F \cosh\left(\frac{3q_3 \Sigma_m}{2\Sigma_y}\right) - (q_4 + (q_2 F)^2) = 0, \tag{48}$$

where again, \tilde{J}_2 is the second invariant of the generalized stress, now given by

$$J_2 = a_1^1 \bar{\boldsymbol{\zeta}}^1 : \bar{\boldsymbol{\zeta}}^1 + a_1^2 \bar{\boldsymbol{\sigma}}^2 : \bar{\boldsymbol{\sigma}}^2 + \frac{a_2^2}{(\ell^2)^2} \bar{\boldsymbol{\sigma}}^2 : \bar{\boldsymbol{\sigma}}^2 + a_1^3 \bar{\boldsymbol{\sigma}}^3 : \bar{\boldsymbol{\sigma}}^3 + \frac{a_2^3}{(\ell^3)^2} \bar{\boldsymbol{\sigma}}^3 : \bar{\boldsymbol{\sigma}}^3 \quad (49)$$

and Σ_y is the generalized yield stress which is a function of the effective generalized plastic strain, Υ_{eff} , where

$$\dot{\Upsilon}_{\text{eff}} = \sqrt{c_1^1 \bar{\mathbf{L}}^1 : \bar{\mathbf{L}}^1 + c_1^2 (\bar{\mathbf{L}}^2 - \bar{\mathbf{L}}^1) : (\bar{\mathbf{L}}^2 - \bar{\mathbf{L}}^1) + c_2^2 (\ell^2)^2 \bar{\nabla} \bar{\mathbf{L}}^2 : \bar{\nabla} \bar{\mathbf{L}}^2 + c_1^3 (\bar{\mathbf{L}}^3 - \bar{\mathbf{L}}^1) : (\bar{\mathbf{L}}^3 - \bar{\mathbf{L}}^1) + c_2^3 (\ell^3)^2 \bar{\nabla} \bar{\mathbf{L}}^3 : \bar{\nabla} \bar{\mathbf{L}}^3} \quad (50)$$

Σ_m is a generalized hydrostatic stress measure given by

$$\Sigma_m = b_1^1 \bar{\sigma}_m^1 + b_1^2 \bar{\sigma}_m^2 + \frac{b_2^2}{(\ell^2)^2} \bar{\sigma}_m^2 + b_1^3 \bar{\sigma}_m^3 + \frac{b_2^3}{(\ell^3)^2} \bar{\sigma}_m^3, \quad (51)$$

where subscript m represents a hydrostatic quantity. ℓ^2 and ℓ^3 are length scales which are characteristic of the micro and submicroscales respectively. For a square averaging domains in 2 dimensions, $A_{\Omega^2} = \ell^2 \times \ell^2$, where A_{Ω^2} is the area of the microaveraging domain, Ω^2 , and $A_{\Omega^3} = \ell^3 \times \ell^3$, where A_{Ω^3} is the area of the submicroaveraging domain, Ω^3 . F is a general measure of void volume fraction given by

$$F = d^1 \bar{f}^1 + d^2 (\bar{f}^2 - \bar{f}^1) + d^3 (\bar{f}^3 - \bar{f}^2) \quad (52)$$

where the average values of void volume fraction at each scale are given by the appropriate f measure.

3.4.4. Determination of constants: multiresolution cell modeling

Various material constants are evident in the above relationships. By examining the average behavior at each scale (Fig. 15) these constants can be determined. Due to the complexity of the response, a computational cell modeling technique is applied to determine the local stress and deformation fields at each scale. When examining the behavior at a particular scale, the average deformation at the larger scales can be considered to be zero and the average deformation at the lower scales can be considered equal to the scale of interest. For example, when looking at the microscale, $\alpha = 2$, the average macrodeformation rate, $\bar{\mathbf{L}}^1$, is zero and the average sub-microdeformation rate, $\bar{\mathbf{L}}^3$, is equal to the average microdeformation rate, $\bar{\mathbf{L}}^2$. In that case, Eq. (50) simplifies to

$$\dot{\Upsilon}_{\text{eff}} = \sqrt{c_1^2 (\bar{\mathbf{L}}^2) : (\bar{\mathbf{L}}^2) + c_2^2 (\ell^2)^2 \bar{\nabla} \bar{\mathbf{L}}^2 : \bar{\nabla} \bar{\mathbf{L}}^2 + c_1^3 (\bar{\mathbf{L}}^2) : (\bar{\mathbf{L}}^2) + c_2^3 (\ell^3)^2 \bar{\nabla} \bar{\mathbf{L}}^2 : \bar{\nabla} \bar{\mathbf{L}}^2}. \quad (53)$$

The generalized constitutive relationship, Φ , reduces to the average microconstitutive relationship Φ^2 .

Fig. 16 shows how the constitutive relationship is found by examining each scale individually. The submicroaveraging domain, Ω^3 , is explicitly modeled using a J_2 -type material for the metal matrix and suitable material properties for the strengthening particles and the debonding energy. The size of the averaging domain is chosen to capture the interactions which characterize the micromechanics at that scale. Boundary conditions are applied, giving rise to an average sub-microdeformation rate, $\bar{\mathbf{L}}^3$, and average sub-microdeformation rate gradient, $\bar{\nabla} \bar{\mathbf{L}}^3$. These average measures are evaluated using Eq. (2). The length scale of the averaging domain is thereby implicitly embedded in the constitutive law.

Different displacement boundary conditions will result in a different response in the averaging domain. The average response can be determined in terms of the boundary conditions by using the divergence theorem to find the average stress and deformation measures over the averaging domain at the α th scale:

$$\bar{\boldsymbol{\sigma}}^\alpha = \frac{1}{V_{\Omega^\alpha}} \int_{\Omega^\alpha} \boldsymbol{\sigma} dV = \frac{1}{2V_{\Omega^\alpha}} \int_{S^\alpha} \boldsymbol{\sigma} \cdot \mathbf{n} \otimes \mathbf{x} dS, \quad (54)$$

$$\bar{\mathbf{L}}^\alpha = \frac{1}{V_{\Omega^\alpha}} \int_{\Omega^\alpha} \mathbf{L} dV = \frac{1}{2V_{\Omega^\alpha}} \int_{S^\alpha} (\mathbf{v} \otimes \mathbf{n} + \mathbf{n} \otimes \mathbf{v}) dS, \quad (55)$$

where V_{Ω^α} is the volume and S^α is the surface of the averaging domain at the α th scale of interest. $\boldsymbol{\sigma} \cdot \mathbf{n}$ is the surface traction, \mathbf{v} is the velocity and \mathbf{n} is a unit normal to the surface. The average deformation gradient and higher order stress at each scale are found in a similar manner. By varying the displacement boundary conditions and computing the average submicrostress, $\bar{\boldsymbol{\sigma}}^3$, and its first moment, $\bar{\boldsymbol{\sigma}}^3$, it is possible to characterize the constitutive relationship, Φ^3 , at the submicroscale. The material constants associated with the submicroterms in Eqs. (49)–(51) are determined.

The relationship submicrorelationship Φ^3 is subsequently used to represent the matrix material behavior at the microscale. This time the microaveraging domain, Ω^2 , which contains inclusions is explicitly modeled. The process is repeated to find the relationship Φ^2 and hence more material constants are defined. The relationship between $\bar{\mathbf{L}}^1$ and $\bar{\boldsymbol{\sigma}}^1$ can be determined by examining the average behavior of an RVE. The material within the RVE is described by the constitutive behavior which was determined at the microscale i.e. the average behavior over Ω^2 is used to represent a point in the RVE. The final unknown material constants are found and the generalized constitutive law is defined.

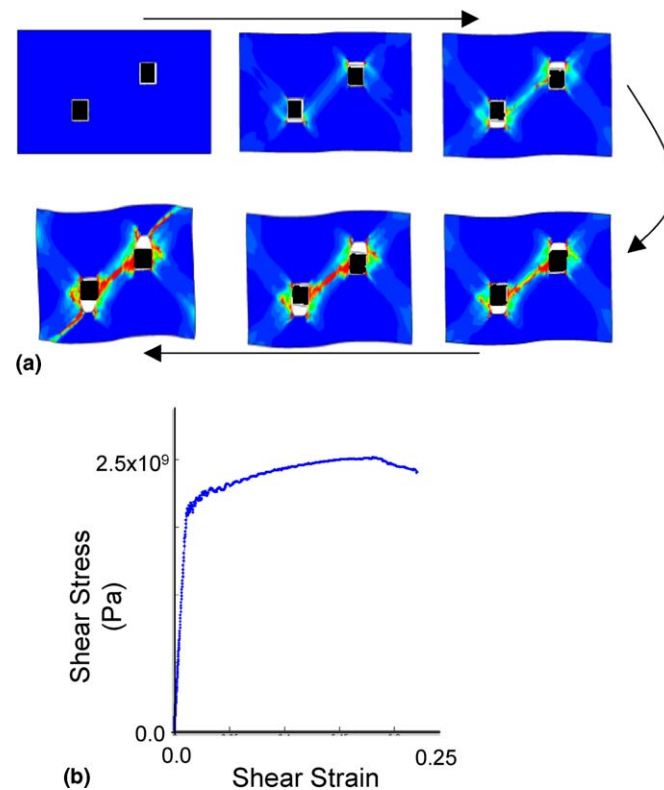


Fig. 17. Simulated void fraction contours in a loaded sample. (a) Microscale softening in pure shear [15]. Even in pure shear, a localized hydrostatic component of stress arises between two inclusions. Subsequently, the strengthening particles in this region debond. Voids nucleate and grow, causing the softening shown in (b).

In this way, the properties of a metal alloy containing two populations of particles can be determined. Each scale will undergo varying levels of softening depending on the average amount of damage at that particular scale. However, there is also a degree of interaction between the scales. For example, even if the macrodeformation, $\bar{\mathbf{L}}^1$, is zero and the average microdeformation rate, $\bar{\mathbf{L}}^2$, is a pure shear quantity, the overall constitutive response will still show a softening effect. Softening generally only occurs under hydrostatic loading. This can be explained by examining the submicroscale. An average hydrostatic stress field occurs at the submicroscale due to localization between the microscale particles. This leads to void nucleation and growth at the submicroscale. This is illustrated in Fig. 17 for a microscale domain subjected to a pure shear deformation. The stress field between the two microscale inclusions has a hydrostatic component. The material within the localized stress field contains submicroscale strengthening particles. This material is represented by a Gurson-like material law [11] derived by studying the average response of a submicroscale averaging domain. Fig. 17 shows that the average shear response over the microscale domain displays a softening regime. This directly corresponds to the void sheet mechanism described before.

The multiresolution response can therefore be used in conjunction with multiresolution cell modeling to derive a generalized constitutive law bereft of any empiricism. The properties can be determined in terms of the microstructural architecture which is explicitly modeled in the averaging domain at each scale. The effect of inter and intra scale interactions is captured in the generalized constitutive law. Hence, the properties are fully described in terms of the microstructure, presenting an opportunity for microstructure design and optimization.

3.5. Bio-inspired self-healing composites

The notion of ‘self-healing’ materials originates in biomimesis, the study and design of high-tech products that mimic biological systems. This technology is expected to have a huge application range from microelectronics to aerospace, where unchecked damage could lead to massive failure. It has been predicted that ‘*the day may come when cracks in buildings or in aircraft structures close up on their own, and dents in car bodies spring back into their original shape*’ [28]. In general, self-healing is the ability of a material to restore mechanical properties, which were earlier perturbed by a plastic deformation or failure involving cracks and voids. Investigation of possible self-healing mechanisms is an important emerging field.

Self-healing technologies could have a massive impact on various industries by reducing maintenance requirements, increasing safety and product lifetime. Researchers envision autonomous devices, medical implants, sensors, and even space vehicles that, similar to biological organisms, would have the ability to identify and subsequently heal damage in their mechanical function. Particularly, these structures could be used in applications where repair is impossible or impractical, e.g., in implanted medical devices, electronic circuit boards and aerospace/space systems. One recent application of bio-inspired self-healing materials has been the development and analysis of composites with shape memory alloy (SMA) inclusions [29–33]. The unique behavior of shape memory alloys is due to a reversible thermo-elastic phase transformation between martensite and austenite.

3.5.1. SMA overview

The SMA parent phase, austenite, displays a cubic crystal lattice structure (Fig. 18a). In the absence of an applied load, upon cooling the austenite transforms into another stable phase, ‘self-accommodated’ martensite, (Fig. 18b). Different variants of martensite form which are all crystallographically equivalent, but with differing spatial orientation. In self-accommodated martensite, no observable macroscopic deformation occurs because all variants (usually 24 habit plane variants for a particular twinning system) appear equally when martensite is formed by cooling. Upon heating the transformation is fully reversible. Four temperatures are associated with the transformation:

- Martensitic start temperature (M_s)—the temperature at which the material starts transforming from austenite to martensite.
- Martensitic finish temperature (M_f)—signifies the transformation is complete i.e. the material is fully martensitic.
- Austenite start temperature (A_s)—the reverse transformation begins.
- Austenite finish temperature (A_f)—the reverse phase transformation is completed and the material is the austenitic phase.

If a load is applied to the martensite (at constant temperature) the crystallographic twinned structure will reorient to variants preferred by the load direction. This reorientation leads to a ‘detwinned’ martensitic structure and an associated macroscopic strain (Fig. 18c). Assuming no change in temperature, the macroscopic strain remains constant during unloading; an analogous process to a plastic deformation. However, this strain can be reversed through a temperature-induced phase transformation back to the austenite phase (Fig. 18d). Steps b–c–d (load–unload–heat) form the basis of the shape memory effect (SME).

If the austenite phase material is loaded, the material will deform through a stress-induced phase transformation to martensite. As the stress required for this phase transformation is higher than that required for reorientation an appropriate

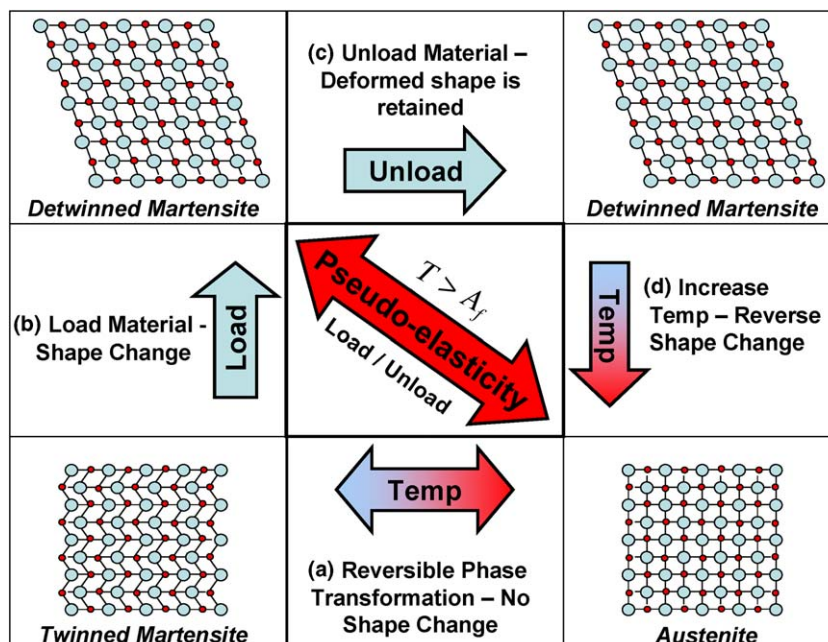


Fig. 18. (a)–(d) SMA overview shows the shape memory effect and pseudo-elasticity.

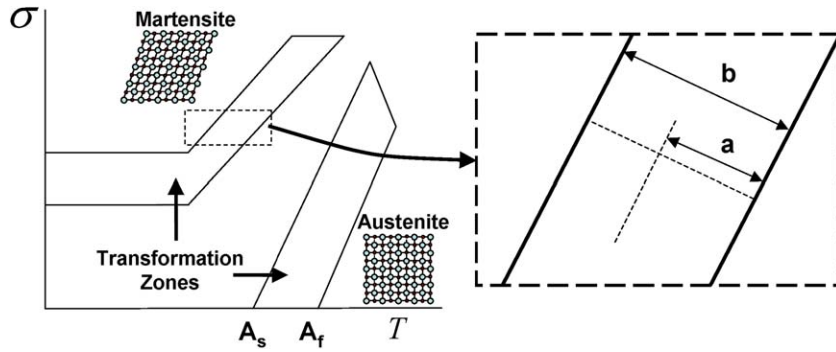


Fig. 19. A stress–temperature map of austenite and martensite transformation zones. The martensite and austenite start and finish times are modeled as linearly related to the applied load. At lower temperatures, the transformation behavior is controlled by the applied load only.

precipitate structure is necessary to impede dislocation motion. As in reorientation, an oriented martensitic structure is formed with an associated macroscopic strain. Upon unloading the reverse transformation occurs as the martensite is no longer stable at the elevated temperature; indeed the transformation temperatures are often modeled as being linearly related to the applied load (Fig. 19). This elevated temperature load–unload cycle is often called “pseudoelasticity” or “superelasticity”.

3.5.2. SMA one-dimensional constitutive law

The 1-d SMA constitutive model is based on a model by Tanaka et al. [34], modified by Liang and Rogers [35] and subsequently by Brinson [36], Brinson and Huang [37] and Bekker and Brinson [38]. The volume fraction of the martensite phase is related to the material stress and temperature history. Fig. 20 shows a stress–temperature phase diagram of the austenite and martensite transformation zones for a typical SMA. The material is considered to be composed of a fraction of austenite and a fraction of martensite. Within the martensite transformation zone, the fraction of martensite is related to the stress–temperature path history and the ratio $\frac{a}{b}$, the relative distance across the transformation zone. The martensite volume fraction increases when moving across the martensite transformation zone in the direction from the M_s side to the M_f side. In the reverse manner, the martensite fraction decreases in the austenite transformation zone.

The flow stress of the SMA is then related to the fraction of martensite by

$$\sigma = E(\varepsilon - \varepsilon_L \zeta_s) + \Theta \Delta T, \quad (56)$$

where E is the elastic modulus, ε is the strain, ε_L is the maximum transformation strain, ζ_s is the stress-induced martensite fraction, Θ is related to the thermal expansion coefficient and T is the temperature. A kinetic law [38] is coupled with Eq. (56) to determine the value of ζ_s via a phase diagram kinetics approach using Fig. 19 as briefly described above.

3.5.3. Bone-shaped short (BSS) fibers

The use of relatively ductile bone-shaped short (BSS) fibers to geometrically reinforce brittle materials has proved capable of improving both strength and toughness significantly [39–42]. Those papers have shown that use of BSS fibers

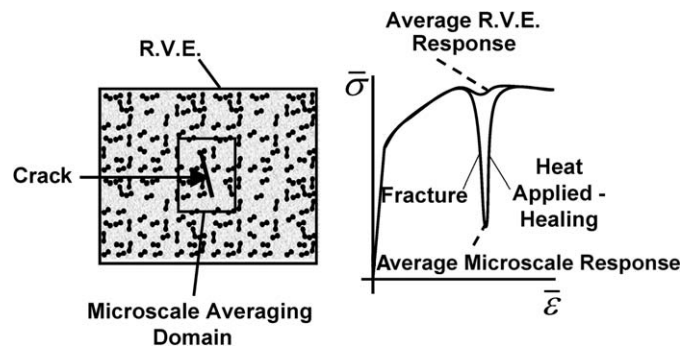


Fig. 20. The average microbehavior is more extreme than the average macrobehavior. The graph shows the stress and strain averaged over each domain. The crack causes severe average fracture behavior over the microscale domain shown. However when the average behavior of the RVE is considered, the resulting average fracture is much less severe. The healing effect is also more pronounced at the microscale.

maximized energy dissipation through fiber debonding and matrix deformation yet avoided complete fracture by prohibiting fiber pullout. The BSS fibers bridged the crack and resisted crack opening and further propagation. A weak interface that debonds is essential in order to take advantage of the crack bridging capabilities. Thus, the presence of BSS fibers will provide superior energy dissipation by crack bridging, debonding and crack deflection. If the BSS fiber is composed of a shape memory alloy, the enforced phase transformation which occurs during crack bridging will also cause some energy dissipation. In addition, by using a shape memory alloy (SMA) for the bone-shaped inclusion material, it is possible to produce a self-healing composite by taking advantage of the shape memory properties of the inclusions. Subsequent to loading, the composite can be heated. This causes the matrix material to become softer and a reverse phase transformation within the inclusions leads. The BSS fibers attempt to return to their original shape, closing up any small microcrack in the softened material in the process.

The behavior at the microscale differs from the macroscale behavior during both the deformation and healing stages as shown schematically in Fig. 20. In Fig. 20 a crack develops at the microscale. The material is subsequently heated causing the BSS fibers to shrink and close the crack. The material can again sustain a load. The *average* fracture behavior and healing effect over the microscale region is invariably more extreme than that over the macroscale region. The profound effects of localized deformation and material healing are thus lost through macroscale averaging.

The composite can be resolved to two scales: the macroscale and the microscale. The healing effect is a microscale event. The microaveraging domain contains a population of SMA BSS fibers. For simplicity, the BSS fibers are modeled as having elastic ends joined together by an SMA rod. In this way, the 1-d SMA constitutive law can be applied to the rod, without losing the important mechanics. Contact between the BSS fiber and the matrix is modeled as hard contact with a nonlinear elastic law representing the interfacial debonding. Interfacial debonding occurs at the elastic limit of the matrix material i.e. the interface is modeled as being weakly bonded. An averaging domain is simulated which captures the interactions between BSS fibers and the geometrical crack bridging mechanism. The average microscale constitutive behavior can be examined over this domain. The matrix material is considered to be elastic–plastic with some strain softening due to accumulated plastic strain and also temperature softening. A typical microaveraging domain is illustrated in Fig. 21.

With reference to Fig. 22a, during loading the BSS fibers succeed in geometrically strengthening the material and the martensite fraction increases in the loaded BSS fibers. Energy is dissipated through the mechanisms described above. The bridging effect of the SMA BSS fibers is evident by comparing the average constitutive behavior of the microaveraging domain with fibers and a microaveraging domain without fibers (dotted line in Fig. 22a). Upon unloading, the elastic strain is released and a residual average plastic strain remains. During the subsequent heating phase the fraction of martensite decreases and the BSS fibers attempt to return to their original size. From Fig. 22b, the reduction in strain caused by fiber ‘shrinkage’ is most pronounced in the temperature range 130–150 °F which coincides with austenite transformation zone. During cooling the average strain in the microdomain decreases to below 0.001 and finally levels off at a value below 0.002. A second load, unload, heat and cool cycle results in a hysteresis type average behavior at the microscale. However, each successive cycle results in a greater value of the residual plastic strain, ε_C , and a reduction in material strength, σ_C , due to damage accumulation in the matrix material (Fig. 22b).

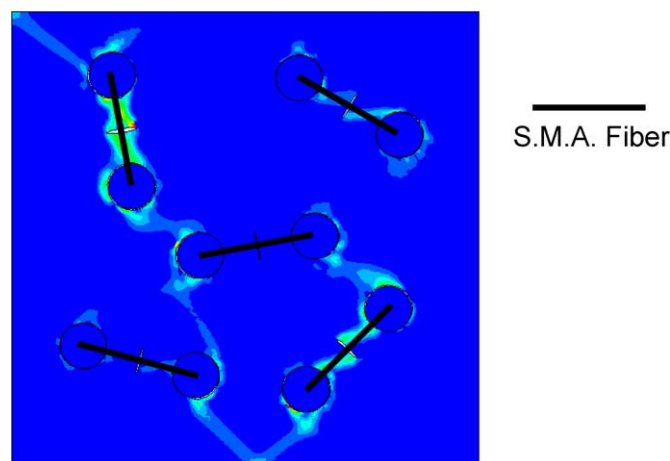


Fig. 21. Simulated microaveraging domain of a composite containing shape memory alloy (SMA) bone-shaped short (BSS) fibers modeled as two elastic spheres joined a SMA fiber. Plastic strain contours are shown. The fiber volume fraction is 0.08.

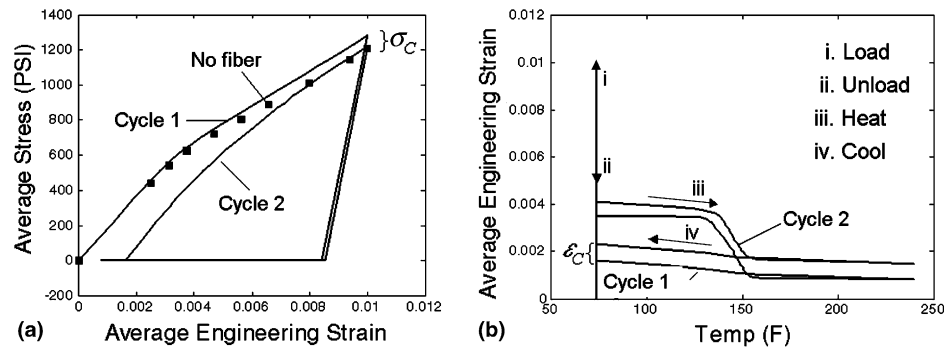


Fig. 22. (a) Stress vs strain; (b) Strain vs temperature for the microaveraging domain. A hysteresis-type behavior is evident.

The crack bridging and healing effect of the BSS fibers can be considered as a process which is predominant at the microscale. The multiresolution approach can therefore capture the localized deformation and healing effect through an average microscale constitutive relation, Φ^2 which describes the behavior shown in Fig. 22. The macroscale average behavior, Φ^1 , can be determined by examining the average behavior of an RVE. The material within the RVE is characterized by the predetermined microscale constitutive relationship, Φ^2 . A generalized constitutive law, Φ , can be formed by combining the constitutive laws at each scale. When localization occurs, it becomes much more severe due to the *microdeformation* contribution. On the other hand, the healing effect within the localized region will be more pronounced due to the contribution from the microscale healing. Both of these microscale phenomena are captured in the microscale part of the generalized constitutive relation. The healing properties can then be determined in terms of the key microstructural parameters such as fiber size and spacing.

4. Conclusion

The proposed multiresolution technique is capable of linking overall material properties to the underlying microstructure via the micromechanics at each scale of interest. The small-scale deformation phenomena which have a profound impact on macroscale properties are captured. The technique is general enough to be used in any material which exhibits different constitutive behavior at each scale. It can be implemented in a general finite element framework. The method has been successfully applied to a granular material, a porous material and a polycrystalline material with dislocations. The multiresolution approach has the potential to elucidate the properties of complex materials such as an alloy with two scales of particles and theoretical self-healing composites through computational cell modeling.

In terms of material design, the multiresolution approach is a method capable of describing the crucial link between material microstructure and properties, and offers the exciting prospect of eliminating the need for expensive and time consuming mechanical testing and prototyping. As industry is pushing for lighter and stronger materials, the multiresolution theory offers an opportunity for optimization of properties in terms of microstructural architecture. Within the current framework, we hope to examine complex systems such as lightweight magnesium alloys and study the micromechanics of aluminum alloys in more detail. The predictive capabilities of the theory can also aid the rapid advancement of bio-inspired self-healing composites, which are currently in their infancy. Advance knowledge of the optimum microstructure of these next generation composites is crucial when seeking a capable fabrication process. In theory, many complex materials can be designed and optimized through this technique before a fabrication process has even been designed.

Acknowledgements

The authors acknowledge the support of the Office of Naval Research. Wing Kam Liu also acknowledges the support of the National Science Foundation.

References

- [1] A. Borrego, R. Fernandez, M. del Carmen Cristina, J. Ibanez, G. Gonzalez-Doncel, Influence of extrusion temperature on the microstructure and the texture of 6061Al–15 vol.% SiCw PM composites, *Compos. Sci. Technol.* 62 (2002) 731–742.
- [2] P.T. Wang, W.H. Van Geertruyden, W.Z. Misiolok, Proceedings from Materials Solutions Conference 2003: 1st International Symposium on Metallurgical Modeling for Aluminum Alloys, 2003, pp. 199–208.
- [3] A.J. Brand, S. Kalz, R. Kopp, Microstructural simulation in hot rolling of aluminium alloys, *Computat. Mater. Sci.* 7 (1996) 242–246.
- [4] K.F. Karhausen, F. Roters, Development and application of constitutive equations for multiple-stand hot rolling of Al-alloys, *J. Mater. Process. Technol.* 123 (2002) 155–166.

- [5] C.M. Sellars, Q. Zhu, Microstructural modeling of aluminium alloys during thermomechanical processing, *Mater. Sci. Engrg.* A280 (2000) 1–7.
- [6] M.A. Sutton, B. Yang, A.P. Reynolds, R. Taylor, Microstructural studies of friction welds in 2024-T3 aluminum, *Mater. Sci. Engrg. A* 323 (2002) 160–166.
- [7] T. Belytschko, W.K. Liu, B. Moran, *Nonlinear Finite Elements for Continua and Structures*, John Wiley, Chichester, New York, 2000.
- [8] S. Li, W.K. Liu, *Meshfree Particle Methods*, Springer, Berlin, 2004.
- [9] D.J. Bammann, M.L. Chiesa, G.C. Johnson, Modeling large deformation and failure in manufacturing processes, *Proc. 19th ICTAM* (1996) 359–378.
- [10] M.F. Horstemeyer, S. Ramaswamy, M. Negrete, Using a micromechanical finite element parametric study to motivate a phenomenological macroscale model for void/crack nucleation in aluminum with a hard second phase, *Mech. Mater.* 35 (2003) 675–687.
- [11] A.L. Gurson, Continuum theory of ductile rupture by void nucleation and growth: Part I—Yield criteria and flow rules for porous ductile material, *J. Engrg. Mater. Technol.* 99 (1997) 2–15.
- [12] S. Hao, W.K. Liu, C.T. Chang, Computer implementation of damage models by finite element and meshfree methods, *Computat. Methods Appl. Mech. Engrg.* 187 (2000) 401–440.
- [13] S. Hao, W.K. Liu, B. Moran, F. Vernerey, G.B. Olson, Multi-scale constitutive model and computational framework for the design of ultra-high strength, high toughness steels, *Comput. Methods Appl. Mech. Engrg.* 193 (17–20) (2004) 1865–1908.
- [14] Z.P. Bazant, Nonlocal integral formulations of plasticity and damage: Survey of progress, *J. Engrg. Mech.* 128 (11) (2002) 1119–1149.
- [15] F. Vernerey, W.K. Liu, B. Moran, Northwestern University, Illinois, in preparation.
- [16] N.A. Fleck, G.M. Muller, M.F. Ashby, J.W. Hutchinson, Strain gradient plasticity: theory and experiment, *Acta Metall. Mater.* 42 (2) (1994) 475–487.
- [17] J.S. Stolken, A.G. Evans, Microbend test method for measuring the plasticity length scale, *Acta Mater.* 46 (14) (1998) 5109–5115.
- [18] W.D. Nix, R.F. Mehl Medalist, Mechanical properties of thin films, *Metall. Trans. A (Phys. Metall. Mater. Sci.)* 20(A) (11) (1989) 2217–2245.
- [19] N.A. Fleck, J.W. Hutchinson, Strain gradient plasticity, *Adv. Appl. Mech.* 33 (1997) 296–358.
- [20] H. Gao, Y. Huang, W.D. Nix, J.W. Hutchinson, Mechanism-based strain gradient plasticity theory, *J. Mech. Phys. Solids* 47 (1999) 1239–1263.
- [21] S.H. Chen, T.C. Wang, A new hardening law for strain gradient plasticity, *Acta Mater.* 48 (2000) 3997–4005.
- [22] T.M. Knowlton, J.W. Carson, G.E. Klinzing, W.-C. Yang, The importance of storage, transfer, and collection, *Chem. Engrg. Progr.* 90 (4) (1994) 44–54.
- [23] H. Kadowaki, W.K. Liu, Bridging Multiscale method for localization problems, *Comput. Methods Appl. Mech. Engrg.* 193 (2004) 3267–3302.
- [24] Z.P. Bazant, T.B. Belytschko, T. Chang, Continuum theory for strain softening, *J. Engrg. Mech.* 110 (12) (1984) 1666–1692.
- [25] G. Green, J.F. Knot, Initiation and propagation of ductile fracture in low strength steels, *J. Engrg. Mater. Technol.* 98 (1976) 37–46.
- [26] M.F. Horstemeyer, M.M. Matalanis, A.M. Sieber, M.L. Botos, Micromechanical finite element calculations of temperature and void configuration effects on void growth and coalescence, *Int. J. Plast.* 16 (2000) 979–1015.
- [27] B.I. Edelson, W.M. Baldwin Jr., Effect of second phases on mechanical properties of alloys, *ASM Trans.* 55 (1) (1962) 230–250.
- [28] SRI Consulting Business Intelligence, *Next-Generation Technologies: Self-Repairing Structural Materials*, 2004. Available from: <www.sric-bi.com>.
- [29] B.S. Files, Design of a biomimetic self-healing superalloy composite, *Materials Science and Engineering*, Evanston, Northwestern University, 1997.
- [30] C. Forbell, M. Barney, C. Scharff, W. Lai, Tin Based Self-Healing Alloy, Student Design Team, Northwestern University, 1997.
- [31] A. Shimamoto, J. Nam, Effect of crack closure by shrinkage of embedded shape-memory TiNi fiber epoxy composite under mixed-mode loading, *Int. J. Mater. Product Technol.* 1 (2001) 263–268.
- [32] X. Gao, D. Burton, L.C. Brinson, Finite element simulation of a self-healing shape memory alloy composite, *Mech. Mater.*, in press.
- [33] K. Hamada, F. Kawano, Shape recovery of shape memory alloy fiber embedded resin matrix smart composite after crack repair, *Dental Mater. J.* 22 (2) (2003) 160–167.
- [34] K.S. Tanaka, S. Kobayashi, Y. Sato, Thermomechanics of transformation pseudoelasticity and shape memory effect in alloys, *Int. J. Plast.* 2 (1) (1986) 59–72.
- [35] C. Liang, C.A. Rogers, One-dimensional thermomechanical constitutive relations for shape memory materials, *J. Intell. Mater. Syst. Struct.* 1 (2) (1990) 207–234.
- [36] L.C. Brinson, One-dimensional constitutive behavior of shape memory alloys: thermomechanical derivation with non-constant material functions, *J. Intell. Mater. Syst. Struct.* 4 (2) (1993) 229–242.
- [37] L.C. Brinson, M.S. Huang, Simplifications and comparisons of shape memory alloy constitutive models, *J. Intell. Mater. Syst. Struct.* 7 (1) (1996) 108–114.
- [38] A. Bekker, L.C. Brinson, Phase diagram based description of the hysteresis behavior of shape memory alloys, *Acta Mater.* 46 (10) (1998) 3649–3665.
- [39] H. Jiang, J. Valdez, Strength and toughness of cement reinforced with bone-shaped steel wires, *Compos. Sci. Technol.* 60 (9) (2000) 1753–1761.
- [40] Y.T.T. Zhu, I.J. Beyerlein, Bone-shaped short fiber composites—an overview, *Mater. Sci. Engrg. A—Struct. Mater. Prop. Microstruct. Process.* 326 (2) (2002) 208–227.
- [41] Y.T.T. Zhu, I.J. Beyerlein, Issues on the design of bone-shaped short fiber composites, *J. Adv. Mater.* 35 (2) (2003) 51–60.
- [42] Y.T.T. Zhu, I.J. Beyerlein, J.A. Valdez, T.C. Lowe, Fracture toughness of a composite reinforced with bone-shaped short fibers, *Mater. Sci. Engrg. A* 317 (1–2) (2001) 93–100.
- [43] W.K. Liu, E.G. Karpov, S. Zhang, H.S. Park, An introduction to computational nanomechanics and materials, *Comput. Methods Appl. Mech. Engrg.* 193 (17–20) (2004) 1529–1578.
- [44] E. Cosserat, F. Cosserat, *Theorie des Corps Deformable*, A Hermann et Fils, Paris, 1909.
- [45] H. Kadowaki, W.K. Liu, A multiscale approach for the micropolar continuum model, *Comput. Model. Engrg. Sci.* 7 (3) (2005) 269–282.
- [46] H.S. Park, W.K. Liu, An introduction and tutorial on multiple-scale analysis in solids, *Comput. Methods Appl. Mech. Engrg.* 93 (7–20) (2004) 1733–1772.
- [47] W.K. Liu, R.A. Uras, Y. Chen, Enrichment of the finite element method with the reproducing kernel particle method, *J. Appl. Mech. ASME* 64 (1997) 861–870.
- [48] G.J. Wagner, W.K. Liu, Coupling of atomistic and continuum simulations using a bridging scale decomposition, *J. Computat. Phys.* 190 (2003) 249–274.
- [49] T.H. Courtney, *Mechanical Behavior of Solids*, McGraw Hill, Boston, 2000.
- [50] S. Hao, B. Moran, W.K. Liu, G.B. Olson, A hierarchical multi-physics constitutive model for steels design, *J. Comput.-Aided Mater. Des.* 10 (2003) 99–142.

- [51] F.T. Fisher, L.C. Brinson, Viscoelastic behavior of polymer matrix composites with interphase effects: theoretical models and finite element analysis, *Compos. Sci. Technol.* 61 (2001) 731–748.
- [52] R.M. Christensen, A critical evaluation for a class of micromechanics models, *J. Mech. Phys. Solids* 38 (3) (1990) 379–404.
- [53] C. McVeigh, W.K. Liu, Prediction of central bursting during axisymmetric cold extrusion of a metal alloy containing particles, *Int. J. Solids Struct.*, in press.
- [54] H.B. Muhlhaus, I. Vardoulakis, The thickness of shear bands in granular materials, *Geotechnique* 37 (3) (1987) 271–283.